Department of Civil Engineering
Graduate School of Urban Innovation
Yokohama National University

Effect of Sediment Compaction on Wave-induced Pore Pressure Gradients and Morphological Change of a Sandbar

「砂層圧密効果が間隙水圧勾配と沿岸砂州形状変化に及ぼす影響」

By
Md Shofiqul Islam

Supervised by
Professor Takayuki Suzuki

September, 2024

Effect of Sediment Compaction on Wave-induced Pore Pressure Gradients and Morphological Change of a Sandbar

A dissertation submitted in partial fulfillment of the
requirements for the degree
of

Doctor of Philosophy in Engineering

By
Md Shofiqul Islam
Student ID: 21WA906

Examination Committee:
Prof. Takayuki Suzuki (Chair)
Prof. Hiroshi Katsuchi
Prof. Kimitoshi Hayano
Prof. Chikako Fujiyama
Assoc. Prof. Hiroto Higa

Abstract

In coastal areas, understanding the sandbar dynamics is crucial due to their significant contribution to reducing the incident wave energy. Limited research has focused specifically on evaluating sandbar morphology, considering ground-controlling parameters within the sediment bed. Recently, the addition of filling sand in the form of submerged artificial sandbars in the surf zone has been explored as a nature-based solution. To overcome the challenges posed by complex wave-current-sediment interactions in the surf zone, laboratory experiments offer an effective means to closely examine specific parameters. The aim of this study was to analyze the dynamic correlation among wave-induced pore pressure gradients, sediment concentration, and bed-level erosion of a small-scale sandbar under varying compaction conditions. An artificial sandbar of 2 m cross-shore length was positioned on the surf zone of a 17 m long wave flume. A pressure transducers array, concentration meter, wave gauges, and a grid system were installed inside the wave flume. A torque meter was employed to evaluate the precise ground compactness at various depths of the sandbar. A total of sixteen experimental cases of sandbar formation using medium sand (D_{50} = 0.33 mm) and very fine sand (D_{50} = 0.08 mm) were tested.

The experimental results on sandbar morphology revealed that very fine sand was more susceptible to erosion than medium sand in the mechanism of wave breaking to impinging. Sandbars with medium sand exhibited erosion primarily at the offshore sharp end, while those with very fine sand experienced erosion at the impinging point. In loose compaction, medium sand demonstrated a strong inverse correlation (R^2 = 0.80) between net erosion volume and wave steepness, whereas very fine sand exhibited a sharp peak in net erosion volume at medium wave steepness. In medium-dense compaction of very fine sand, the reduction of net erosion volume was 67%, 57%, and 82% at low (0.024), medium (0.041), and high (0.081) wave steepness, respectively. At the middle depth of the sandbar, very fine sand yielded an average increase in shear strength that was five times higher than medium sand. At this depth, a strong inverse correlation ($R^2 = 0.84$) was established between the change in average shear strength and wave steepness under loose compaction of medium sand, however, similar to net erosion volume, a sharp peak was found at the medium wave steepness of very fine sand.

The comprehensive analysis of liquefaction parameters for medium sand showed that the liquefaction index decreased as sediment depth increased. At the same wave height, the decreasing tendency of the liquefaction thickness with increasing wave period was observed. Furthermore, a reduction in wave height resulted in a reduction in the liquefaction thickness. A strong correlation ($R^2 = 0.96$) was established between liquefaction thickness and wave steepness. During the 10 min of wave action, an average of 16.5 % of the liquefied thickness was eroded in loose compaction conditions, whereas 6.3 % of the liquefied thickness was eroded in medium-dense compaction conditions. These findings underscore the importance of sediment compaction in influencing liquefaction potentiality.

In dynamic correlation analysis, the results showed a consistent horizontal pore pressure variation for each experimental case involving medium sand. However, as the sediment depth increased, there was a distinct attenuation in pore pressure amplitude accompanied by a simultaneous rise in the phase lag. Loosely compacted sandbar formations exhibited an average 1.3 times higher maximum vertical pressure gradient than medium-dense compacted formations. The phase-averaged sediment concentration beneath the wave crest was significantly higher than the trough. The erosion volume of the sandbar under loosely compacted conditions exhibited a strong correlation ($R^2 = 0.84$) with the average sediment concentration. A strong dynamic correlation ($R^2 = 0.89$) was established between the maximum phase-averaged vertical pressure gradient and sediment concentration under the same conditions. These significant inter-correlations contribute to enhancing the current understanding of erosion prediction in surf zone sandbars. Ultimately, integrating these insights into beach nourishment strategies can lead to more efficient and sustainable coastal management practices.

Acknowledgments

I begin by offering my utmost gratitude to Allah, the Most Gracious and Merciful, and may His blessings be upon His final Prophet Muhammad (peace be upon him).

I would like to express my deepest appreciation to my supervisor, Prof. Takayuki Suzuki, for his exceptional guidance throughout this research journey. His enduring patience, ready availability, and steadfast support have greatly enhanced both my academic advancement and personal development. Apart from my supervisor, I extend my heartfelt appreciation to Assoc. Prof. Hiroto Higa and Asst. Prof. Martin Mäll for their invaluable insights and words of encouragement, particularly during our weekly laboratory seminar.

I wish to express my profound gratitude to the dissertation committee: Profs. Hiroshi Katsuchi , Kimitoshi Hayano, Chikako Fujiyama, and Assoc. Prof. Hiroto Higa. Their constructive feedback of my research have significantly contributed to refining and strengthening the scientific rigor of this work. Furthermore, I would like to acknowledge the faculty and staff of Yokohama National University. I extend my thanks to the past and present students of the Coastal Engineering lab, including Drs. Salika, Tabasi, Kullarchart, Gelfi, and Takeuchi. I cherish the memories of my Bangladeshi Prof., Q. H. Bari, who has been a guiding influence since my undergraduate studies. I am also deeply grateful for the financial assistance provided by the Monbukagakusho (MEXT) to support my doctoral studies.

To my family, I am particularly grateful to my parents for their constant motivation during the challenging phases of this endeavor. Finally, I want to express my deepest appreciation to my loving wife, as well as my son and daughter, for their unwavering love, encouragement, and support.

Contents

List of Figures

List of Tables

Notation

D_{50}	Median particle size
$\rho_{d\min}$	Minimum dry density
$\rho_{d\max}$	Maximum dry density
τ	Shear strength
$\Delta\tau$	Change in shear strength
ρ_d	Dry density
e	Void ratio
γ_s	Saturated unit weight
γ'	Submerged unit weight
Dr	Relative density
M_{max}	Maximum torque rotation
WGs	Wave gauges
CCM	Conductivity concentration meter
PTs	Pressure transducers
p	Pore water pressure
$\partial p/\partial z$	Vertical pore pressure gradient
$\partial p/\partial x$	Horizontal pore pressure gradient
K_0	Coefficient of earth pressure at rest
Y	Liquefaction index
d_e	Sandbar erosion depth
C_{avg}	Average sediment concentration
C_t	Phase-averaged sediment concentration
ΔV_e	Erosion volume of the sandbar
η	Water level
ξ_0	Surf similarity parameter

Chapter 1

Introduction

1.1 Background

A persistently challenging issue in coastal engineering is related to sediment movement induced by wave breaking, particularly within the surf zone (Madsen, 1974; Tang et al., 2017). In terms of sediment transport, both wave action and the characteristics of the seabed sediment influence its movement. The nearshore morphology changes rapidly due to the complex fluid motions and the resulting sediment suspension and movement (Tabasi et al., 2022). During extreme storms, the sloped alluvial deposits of the estuarine delta are highly susceptible to sediment instability (Yu et al., 2022). This is where sandbars in the surf zone emerge as mitigating features in beach profiles that impact wave dissipation, and ultimately contribute to the protection of coast by changing their shapes and positions (Anderson et al., 2023; Bryan et al., 2019). Their influence on coastal dynamics has led to a shift in focus towards submerged artificial sandbars (SABs) as a nature-based solution for beach protection. Furthermore, hard structures (e.g., groins, sea walls, and breakwaters) for coastal protection result in adverse impacts on the coastal ecosystem in the long run (Hamm et al., 2002).

Recent studies have shown that SABs are not consistent with conventional views of existing sediment dynamics, demonstrating their capacity to induce onshore sediment movement under storm wave conditions (Li et al., 2022). Along with the wave and current conditions, sediment properties such as median grain size and sediment compaction (e.g., low or high) also affect the hydrodynamic properties within the sediment bed (Virtanen et al., 2020; Rijn and Havinga, 1995; Tabasi et al., 2021). However, obtaining detailed field measurements of surf zone sandbars is challenging because of the the complex wave-current-sediment interactions and the periodic motion of sandbars in the cross-shore direction (Mieras et al., 2017; Pape et al., 2010; Zheng et al., 2023). Several hydro-morpho dynamic parameters must be considered to further clarify the phenomenon. Demirci et al. (2014) revealed that prediction of cross-shore sandbar volume relies on an understanding of complex physical relationship between sediment transport rates and other key factors such as waves, currents, base slope, sediment properties, and water depth. In addition, long-term data recording in surf zone is often considered impractical due to time and financial constraints, and the risk of instrument failures. To address this, laboratory experiments are an effective way to closely examine specific parameters under controlled conditions, ensuring complete and reliable datasets for further analysis.

1.2 Objectives of the Research

The main objective of this research was to conduct a comprehensive analysis of the dynamic correlation among wave-induced pore pressure gradients, sediment concentration, and bed-level erosion of a small-scale sandbar under varying compaction conditions. Initially, the effect of wave steepness on wave-induced pore water pressure, sediment concentration, and sandbar morphology under loose and medium-dense compaction conditions was assessed. Subsequently, dynamic inter-correlations were explored by conducting both average and phase-average analyses of datasets, enhancing the understanding of temporal aspects and fluctuations within the complex dynamics governing sandbar erosion. To achieve this main objective, the following specific objectives were formulated.

(1) To investigate the effect of sediment size on sandbar morphology under loose and medium-dense compaction conditions.

(2) To quantify liquefaction parameters for a small-scale surf zone sandbar under varying compaction conditions.

(3) To explore the influence of sediment compaction on wave-induced pressure gradients and sediment concentration of a small-scale sandbar.

1.3 Presentation of the Dissertation

The remainder of the dissertation is organized as follows:

Chapter 2 provides a concise overview of the relevant literature, emphasizing significant findings and recognized limitations that pave the way for the research questions of the present study. Chapter 3 includes detailed descriptions of the experimental setup, instrumentation, sediment properties, and the data processing procedure.

Chapter 4 primarily discusses the influence of sediment size on sandbar morphology under varying compaction conditions. It presents findings regarding local erosion depth and net erosion volume, along with exploring the correlation between changes in shear strength and wave steepness.

Chapter 5 presents the results of the dynamic correlation analysis among key parameters. First section of this chapter is dedicated for the variations in pressure gradients and the attenuation of amplitude combined with its corresponding phase-lag. Second section focuses on the quantitative measurements of liquefaction parameters. The variation of critical liquefaction thickness and sandbar erosion depth in different wave steepness is also presented. Third section focuses on the effect of wave steepness on the average sediment concentration. The inter-correlations among the key parameters of pressure gradient, sediment concentration, and erosion volume are presented in last section. These discussions continue by exploring the dynamic correlation between the maximum phase-averaged vertical pressure gradient and the sediment concentration with the aim of understanding the temporal variation of these parameters.

Finally, Chapter 6 presents the concluding remarks, including the limitations and scope for future research. Following this chapter, the bibliography, appendix, and list of publications offer valuable additional resources.

Chapter 2

Literature Review

A comprehensive overview of essential literature related to sandbar dynamics is presented here. This chapter is divided into three sections, each focusing on key aspects of the current study. Section 2.1 provides an overview of sandbar morphology, discussing the various factors that influence the shape, formation, and evolution of sandbars. Section 2.2 reviews previous research on liquefaction parameters, examining the critical factors that contribute to the liquefaction of sediments. It also explores the governing equations developed to quantify liquefaction index and liquefaction thickness. Finally, the section 2.3 reviews literature on pore pressure responses and sediment concentration. This section aims to provide a comprehensive understanding of how pore pressure gradients and sediment concentration jointly affect sandbar erosion dynamics.

2.1 Sandbar Morphology

Beaches tend to become more prone to storm damage with changes in the dynamic nearshore processes, such as large morphological changes of sandbars (Demirci et al., 2014). As a result of the growing interest from the coastal researchers, extensive efforts have been made to understand the natural shoreface nourishments (Grunnet and Ruessink, 2005; Grasso et al., 2011). Researchers often devote themselves to finding out the effect of the sandbar on the morphological change of beach areas (Anderson et al., 2017;

Li et al., 2022). In terms of sediment transport, under a certain hydraulic loading, grain size of the sediment is a controlling physical property that determines whether a sediment grain moves (Shields, 1936).

The addition of filling sand in the form of submerged artificial sandbar (SAB) in the surf zone has been shown in studies to have the potential not only to reduce incident waves but also to supply sand towards the beach and/or beach-bar area (Pan et al., 2017; Kuang et al., 2021). Li et al. (2022) conducted laboratory experiments on different beach profiles with multiple SAB designs and noted that the artificial sandbar migrates onshore as its bar shape decays, and the stability of the sandbar is controlled by its seaward slope as well as the ratio of crest water depth to bar height. Grasso et al. (2011) observed the shoreface nourishment at different positions of SAB implemented on a barred profile in a wave flume and found that the nourishment in the trough and on the outer bar feeds the bar, and as a result, the bar acts as a wave filter and reduces the erosion of shore. To utilize the above laboratory studies in the field, the compaction of the filling sediment on the sandbar needs to be considered. However, only few works are available in the literature on the behavior of sandbars under different compaction conditions (Tabasi et al., 2021). In addition, the sandbar profile may vary when taking into account the impinging points for different sediment sizes.

2.2 Wave-induced Liquefaction

2.2.1 Past Studies on Wave-induced Liquefaction

Wave-induced liquefaction on the seabed is an important phenomenon for designing offshore and coastal structures such as breakwaters, platforms, pipelines, and anchors, where pore pressure counterbalances the effective stresses in the soil (Kirca and Ulker, 2014; Zen and Yamazaki, 1990). The seabed sediment loses its original strength and undergoes an abrupt change in behavior from being more solid-like to more fluid-like when the accumulated excess pore pressure exceeds the effective stress of the sediment (van Kessel and Kranenburg, 1998). In the past few decades, several studies have investigated the wave-induced liquefaction in the process of pore pressure buildup (Qi and Gao, 2018; Du et al., 2020; Chowdhury et al., 2006; Yu et al., 2022; Wang et al., 2023; Jia et al., 2014; Yang et al., 2019). The analytical findings by Qi and Gao (2018) revealed that the excess pore pressure ratio is recommended for quantitatively assessing the instantaneous degree of liquefaction and depth of influence, particularly when the effective stress is significantly reduced beneath a fully liquefied layer. In addition, their parametric investigations further demonstrated that depth of influence increases with increasing wave height for a specific excess pore pressure ratio, while it decreases with increasing degree of saturation and soil permeability (Qi and Gao, 2018). Du et al. (2020) computed the depth of liquefaction using field data and concluded that their method of calculation of liquefaction depth was appropriate. In a large-scale experiment, Chowdhury et al. (2006) demonstrated that momentary liquefaction depth is governed by wave and seabed properties, and the probability of such momentary liquefaction occurring increases with shorter wave periods. Yu et al. (2022) experimentally concluded that wave-induced liquefied sediment mass originates from the sediment within the liquefied layer, and its motion is significantly influenced by the orbital velocity of wave. In another laboratory experiment, Wang et al. (2023) clarified that sea-bed scour and liquefaction process promote each other by changing sediment transport near the bottom of seabed.

The previous laboratory studies have been conducted with the sediment bed positioned below the wave flume. However, installing the sediment bed on the wave flume and focusing on the effect of wave breaking and bed-level change might lead to varying outcomes. Consequently, assessment of liquefaction can be divided into two phases: the first occurs while the wave breaking has no influence on the sediment bed, and the second occurs when it does. When considering the installation of any coastal structure within the surf zone, the significance of the second phase becomes crucial. Moreover, a clear research gap emerges, as the quantification of liquefaction under various sediment compaction conditions of sandbar has not been thoroughly investigated.

2.2.2 Governing Equations to Quantify Liquefaction

According to McDougal et al. (1989), when the excess pore pressure (Δp) exceeds the maximum excess pore pressure ($\Delta p_{\max}$), liquefaction first emerges. Furthermore, if the quantity of $\Delta p_{\max}$ is equal to the initial average normal stress, the liquefaction criterion can be expressed according to Sumer et al. (2006).

$$\Delta p = \Delta p_{\max} = \frac{1}{3}[\gamma' z(1 + 2k_0)] \tag{2.1}$$

Where $\gamma'(= \gamma_s - \gamma_w)$ is the submerged specific weight of the soil (kN/m^3), k_0 is the coefficient for lateral earth pressure at rest condition, and z is the depth of soil (m) at the level of the pressure transducer.

According to Jia et al. (2014), the degree of stability of soil against liquefaction can be expressed by the liquefaction index (Y).

$$Y = \frac{3\Delta p}{\gamma' z(1 + 2k_0)} \times 100 \tag{2.2}$$

Where Y differs from 0 to 100, and the higher Y means the soil is closer to the liquefied state, and thus more susceptible to erosion and collapse.

According to Yang et al. (2019), the critical liquefaction thickness (z) may be calculated using a formula that is derived from both the equation of liquefaction criterion (i.e., Eq. 2.1) and the equation of excess pore pressure decay.

$$\frac{\gamma_w H}{2\cosh(\lambda h)} e^{-\lambda z} = \frac{1}{3}[\gamma' z(1 + 2k_0)] \tag{2.3}$$

Where λ represents the wavenumbers (m^{-1}), γ_w is the seawater gravity (kN/m^3), H is the wave height (m), and h is the water depth (m).

2.3 Pore Pressure and Sediment concentration

A proper understanding of the pore pressure distribution within the underlying sand layer is necessary for a comprehensive investigation of sandbar morphodynamics. The pore pressure within the underlying sand layer plays a dual role in sediment mobility: an upward force facilitates sediment movement and a downward force hinders it (Sakai and Gotoh, 1996; Suzuki et al., 2009). Previous studies, which often classified seabed configurations using bottom shear stress or Shields numbers, rarely discussed the secondary influence of wave-induced water pressure on sediment movement within a wave field (Sakai and Gotoh, 1996). Based on experimental and theoretical evidence of fluid accelerations in surf zone sediment movement, Madsen and Durham (2007) highlighted the significance of horizontal pressure gradients in driving subsurface sediment movement beneath breaking waves. In a large-scale laboratory experiment, Anderson et al. (2017) demonstrated that both the horizontal and vertical pore pressure gradients influence the initiation of onshore sediment movement beneath steep near-breaking waves in the surf zone, and the magnitude of these gradients during each rotation phase correlates with local wave steepness and relative depth. Li and Gao (2022) validated their experimental findings using a theoretical analysis, confirming the amplitude attenuation and phase lag of the pore pressure phenomena in fine and medium sand beds when waves pass over a porous seabed. Their findings emphasized the combined effects of the wave parameters and soil properties, demonstrating that the phase lag becomes increasingly prominent as the pore pressure amplitude within the seabed attenuates more rapidly.

In a recent study on the effect of history of wave exposures on liquefaction, Sui et al. (2023) concluded that the initial strongest wave climate initiates liquefaction independently of prior exposures, subsequent waves, even with greater properties, do not induce liquefaction. Their findings further showed that while pore pressure may accumulate with stronger subsequent wave climates after the completion of the liquefaction-compaction cycle, it is insufficient to cause liquefaction, or in some cases, the pore pressure may not even build up at all. Upon initiation of liquefaction, seabed particles become prone to entrainment as a fluid under the influence of ocean waves, and periodic responses during a storm sequence stem from two mechanisms: the progressive development of excess pore pressure at the onset of cyclic loading and the generation of oscillatory pore pressure, accompanied by damping amplitude and phase lag (Jeng, 2001). Zhang et al. (2018) determined that the erodibility of fluidized silts leads to the loss of particle cohesive forces, which is highly sensitive to the direction and magnitude of seepage flows. A flume experiment investigated the effects of wave-induced seabed pore pressure on the liquefaction risk, revealing that while short waves had high energy but rapidly decaying high-frequency pressure, long waves carried low energy but effectively propagated low-frequency pressure (Xu et al., 2022). This suggests that relying solely on statistical wave parameters for engineering design may lead to an underestimation of marine geohazards.

Using flow velocity and sediment concentration quantification, Grossmann et al. (2023) showed that during storms, sandbar move offshore owing to breaking-induced flows, and whereas they move onshore during calmer conditions. In a laboratory experiment with non-breaking waves, Tabasi et al. (2021) revealed significant variations in the pore water pressure and sediment concentration due to different sediment compaction levels under the same hydrodynamic conditions. Their findings emphasized the necessity for a comprehensive investigation into the influence of sediment compaction. Understanding the dynamics of surf zone sandbars requires considering complex interactions among waves, currents, sediment properties, and hydro-morpho dynamic factors. Previous studies have highlighted the necessity of comprehensively assessing sediment transport rates alongside factors like base slope and water depth for accurate prediction of cross-shore sandbar volume (Mieras et al., 2017; Pape et al., 2010; Zheng et al., 2023; Demirci et al., 2014). Laboratory experiments are an effective way to closely examine specific parameters under controlled conditions. However, existing research has mainly focused on sediment beds placed beneath wave flumes, without adequately addressing the impact of bed-level erosion caused by breaking waves. Additionally, the temporal relationship between pore water pressure gradients and sediment concentration under varying compaction conditions has not been thoroughly investigated. These significant research gaps, particularly concerning the influence of compaction levels, highlight the necessity for further studies to fully understand sandbar dynamics.

Chapter 3

Methodology

This chapter provides a comprehensive overview of the methodologies utilized to effectively address the research objectives. It begins by outlining the experimental setup for measuring the key parameters, ensuring meticulous attention to detail. Furthermore, the chapter delves into the analysis process. To provide a visual representation of the overall research methodology, Fig. 3.1 is presented, offering readers a coherent framework for understanding the approach taken in this research.

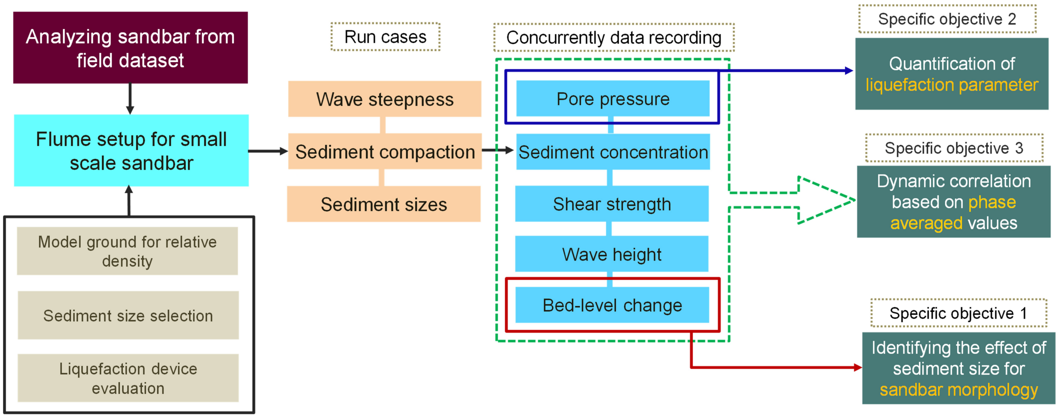

Figure 3.1: Flow chart of the research methodology.

3.1 Laboratory Experiment

3.1.1 Laboratory Scaling

An artificial sandbar was geometrically down-scaled from field observations during the period from 1993 to 1997 on the Hasaki coast, Japan. The variation of the sandbar profiles in field observations are presented in Fig. 3.2. From this observation, 13 cross-shore profiles were selected prior to the storm event to determine various morphometric parameters of the sandbar. Sandbars with heights exceeding 1 m and cross-shore lengths greater than 100 m were considered when determining the morphometric parameters. Details of the morphometric parameters are provided in the Appendix (Table A.1).

The summary of morphometric parameters for both field observations and the laboratory scale sandbar is presented in Table 3.1. In the laboratory setup, the cross-shore length of the sandbar was down-scaled at a ratio of 1:65, while the height of the sandbar was down-scaled at a ratio of 1:10. The decision to employ a trapezoidal shape for the laboratory sandbar was made to ensure a uniform shear strength over the sandbar surface and to consistently position the pressure transducer within the sand. To maintain consistency with the horizontal scale (1:65), the position of the crest in the laboratory sandbar was 3.5 m from the shoreline. The laboratory sandbar exhibited onshore and offshore slopes of 12.5 deg, approximately half of the average slope observed in the field.

Table 3.1: Summary of sandbar morphometric parameters

Morphometric parameters	Field Avg. (St. dev.)	Laboratory scale
Cross-shore length (m)	131.7 (12.28)	2.00
Sandbar height (m)	1.65 (0.23)	0.165
Shoreline to crest distance (m)	215.3 (38.17)	3.50
Water depth above the crest (m)	2.95 (0.54)	0.135
Offshore slope (deg.)	33.7 (7.61)	12.50
Onshore slope (deg.)	26.7 (9.66)	12.50

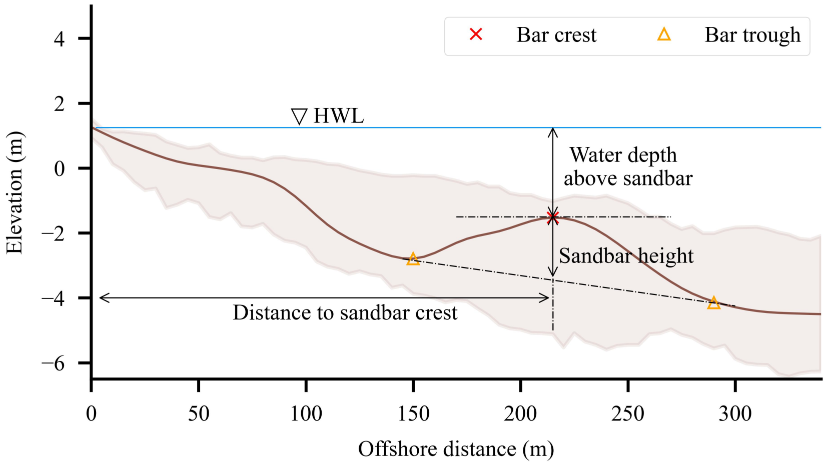

Figure 3.2: Sandbar profile variation from 1993 to 1997. Shaded area indicates the daily profile variations.

3.1.2 Experimental Setup and Instrumentation

Experiments were conducted at the estuarine and coastal engineering laboratory of Yokohama National University using a small-scale wave flume (17 m long and 0.6 m wide), as shown in Fig. 3.3a. The wave flume was equipped with a piston-type wave generator at one end. At the other end of the wave flume, a non-erodible cross-shore beach profile was constructed using a steel frame, maintaining a beach slope of 1:10. Following the down-scaling from field observations, a 200 cm sandbar was constructed using a wooden frame in the surf zone of the flume. A detail pictorial view of flume set-up is outlined in the Appendix (see Fig. A.2).

Four capacitance wave gauges (WGs) were mounted on the wave flume. WG_1 was installed closest to the wave generator (150 cm) to measure the offshore wave characteristics at the laboratory scale. WG_2, WG_3, and WG_4 were installed at the offshore edge, middle, and onshore edge of the sandbar, respectively. All the WGs were connected to a data logger (*Model: midi LOGGER GL900, Graphtec Corporation*). The data logger was set up to record data in Voltage (V) at a frequency of 50 Hz. A conductivity concentration meter (*CCM; Model: PMT5-50, Kenek Co. Ltd.*) was installed in the middle (x = 200 cm), maintaining a 2 cm clear distance above the top surface of

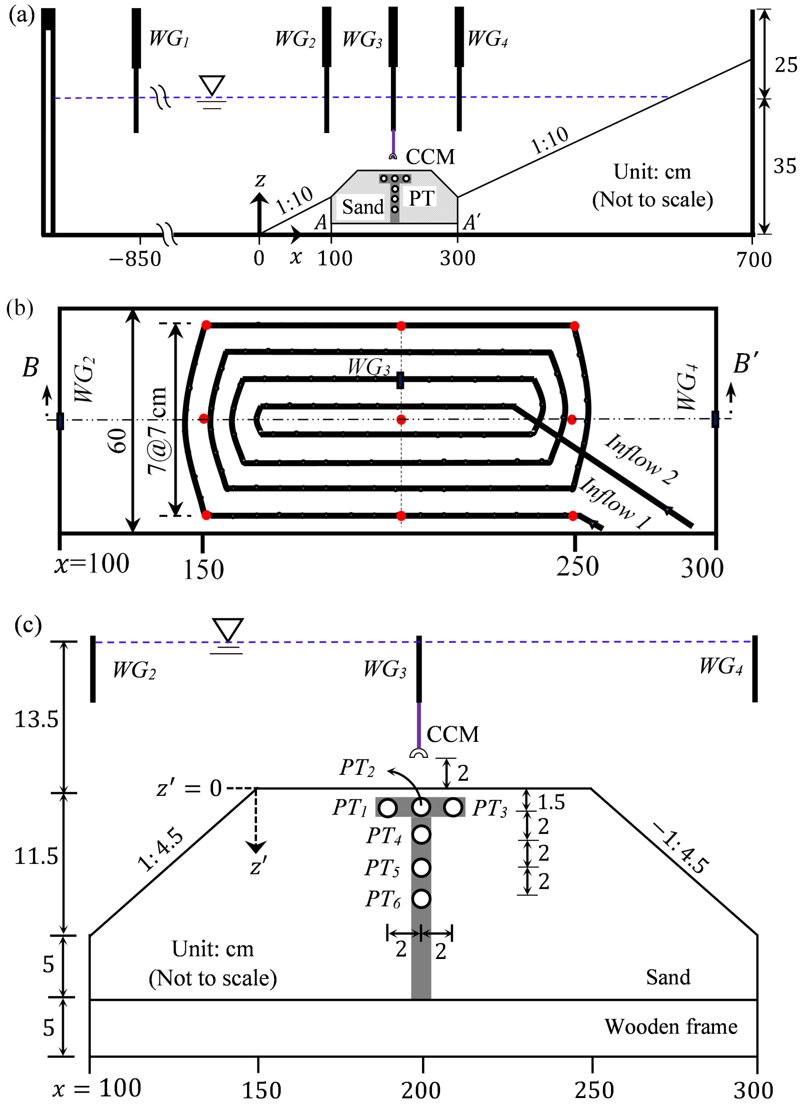

Figure 3.3: (a) Flume setup (b) plan view at the level of *A*-*A*′, and (c) cross-sectional view of *B*-*B*′. The red dot marks the locations of maximum torque rotation measurement. *PT* stands for pressure transducer, *WG* denotes wave gauge, and *CCM* refers to conductivity concentration meter.

sandbar. The concentration meter was connected to the same data logger that was used for the *WGs*. The measuring frequency for the concentration meter was set to match that of *WGs* to enable the concurrent analysis of both wave-related parameters and sediment concentration. The whole data recording unit is outlined in the Appendix (see Fig. A.3).

The sandbar was filled by maintaining a constant falling height of sand and submerged under 35 cm of water. Inside the sandbar sediment, a liquefaction device consisting of a hose pipe was installed at the bottom of the sandbar ($z' = 16.5$ cm) between the cross-shore distance of $x = 150$ and 250 cm, as shown in Fig. 3.3b . The black loop in the Fig. 3.3b indicates plan view of the hose pipe. The spacing of the hose pipe was 7 cm, and small holes (~ 1 mm) were created every 7 cm throughout the length of the hose pipe. Both ends of the hose pipe were connected to a tap for continuous water flow of 2.5 gpm (~ 0.15 L/s) for 5 min to achieve the uniform looseness inside the sandbar. A constant spacing of hole in pipe and a consistent distance between each loop of the pipe, ensuring a nearly homogeneous water pressure distribution on the sediment bed. An overview of the liquefaction device, both before and after its installation, is provided in the Fig. 3.4.

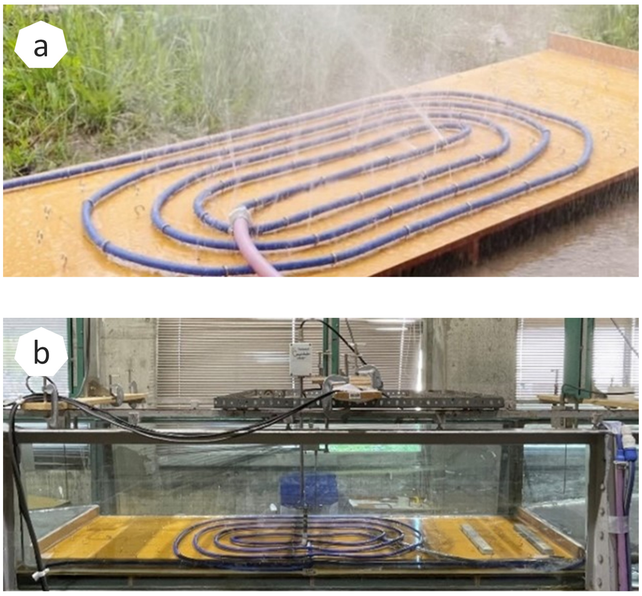

Figure 3.4: Overview of liquefaction device: (a) liquefaction device before setup inside flume and (b) liquefaction device after setup inside flume

To record pore pressure, small-strain-gauge pressure transducers (PTs) or piezoresistive transmitters are frequently used (Pedrozo-Acuña et al., 2011; Suzuki et al., 2010). In this study, pore water PTs were arranged in a

T-shaped array, similar to the experimental setup of Anderson et al. (2017). A T-shaped transducer arrangement was then placed inside the sandbar to measure the pore pressure during the wave action, as shown in Fig. 3.3c. The transducer arrangement consisted of six sensors and one connector (*Sensors: P306A-01, SSK Co. Ltd.; Connector: PCD-400A, Kyowa Electric Co. Ltd.*). The cylindrical transducer heads of the sensor were covered with a steel strainer. The dynamic data acquisition software (*DCS-100A*) was utilized to record data at a frequency of 100 Hz. The horizontal row of the arrangement consisted of three transducers, PT_1, PT_2, and PT_3, which were placed 1.5 cm beneath the top surface of the sandbar. PT_2 was the most common transducer in both directions; the vertical column consisted of four transducers: PT_2, PT_4, PT_5, and PT_6. The transducers were spaced 2 cm center-to-center in both directions. To minimize flow interference, the cables of each transducer were fixed to the flume wall and buried in the sediment. Before the pore-PTs were embedded in the sandbar, they were soaked in water to ensure complete saturation. The pictorial view of this setup is provided in the Appendix (see Fig. A.4.)

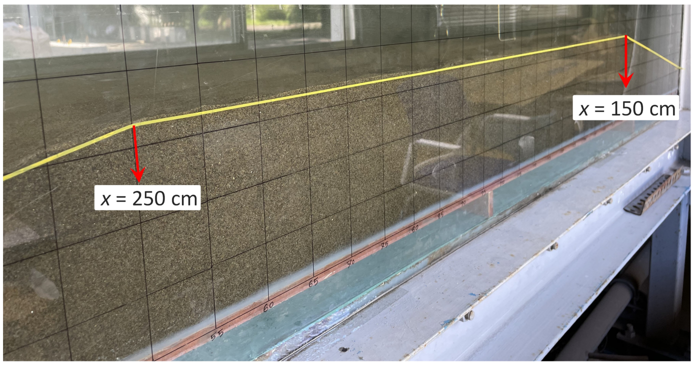

Figure 3.5: A grid system for measuring bed-level change of sandbar.

A grid system (5 cm x 5 cm) was affixed to right side of the glass flume wall, as shown in Fig. 3.5. During the wave action, the bed-level change of the sandbar was monitored using this grid system. In addition to the grid system, the entire experiment were recorded using a video camera. This continuous video recording ensured all aspects of the sandbar's response to wave action.

3.2 Sandbar Sediment Properties

Two different type of silica sand were used to fill the sandbar. The median diameter (D_{50}) of these sediments was 0.33 mm and 0.08 mm, which were classified as medium sand and very fine sand, respectively according to the Udden-Wentworth grain size scale (Udden, 1914; Wentworth, 1922). Fig. 3.6 shows the grain size distribution curve of the sandbar sediment. The coefficient of curvature (C_c) for D_{50} = 0.33 mm and D_{50} = 0.08 mm was 1.15 and 1.25, respectively, while the uniformity coefficient (C_u) for these sediments was 1.89 and 2.22, respectively, classifying them as uniformly graded sand.

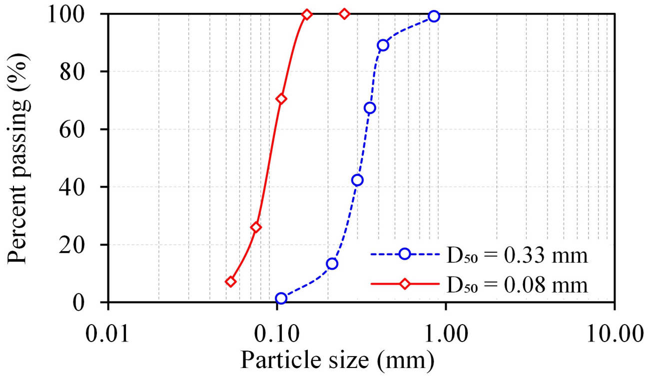

Figure 3.6: Grain size distribution curve of the sandbar sediment.

To assess the maximum and minimum dry density of D_{50} = 0.33 mm, laboratory tests were conducted following to the procedure of JGS 0161-2009, Japanese Geotechnical Society Standard (Japanese Geotechnical Society, 2015), as shown in the Appendix (see Fig. A.5). Furthermore, a model ground (0.445 m long, 0.32 m wide, and 0.15 m high) was constructed to determine the dry density (ρ_d) and relative density (D_r), as shown in Fig. 3.7. The initial state involved filling the model ground with loose sand, which was subsequently submerged under a water head of 35 cm for 5 d to achieve a medium-dense condition. The shear strength of the model ground was measured using a torque meter both before and after 5 d. The maximum torque rotation was recorded at nine different locations, considering three different depths (e.g., z' = 1.5 cm, 7.5 cm, and 15 cm), as shown in Fig. 3.7c. The relative density values of the model ground were determined both initially

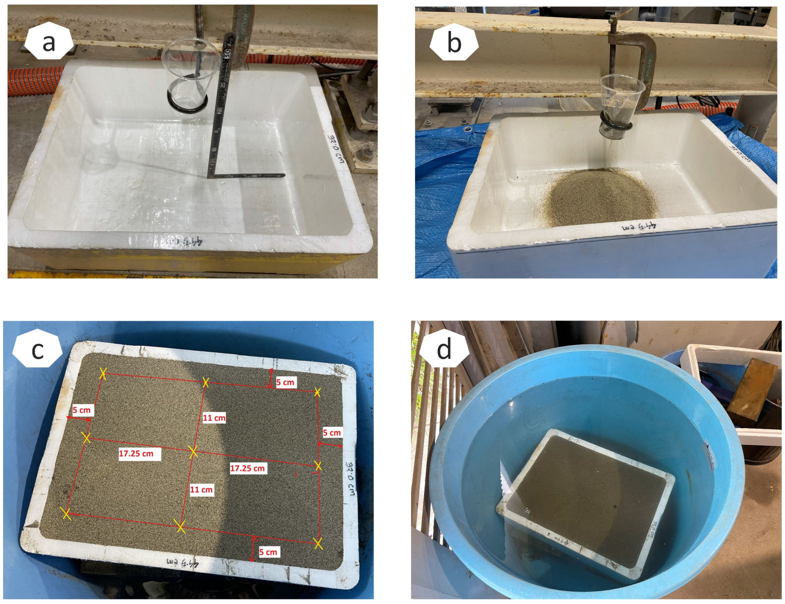

Figure 3.7: Model ground (a) before filling with sand, (b) during filling with sand, (c) torque measuring locations, and (d) under 35 cm water head.

Table 3.2: Summary of properties for sand sample and model ground

(a) Measured from the sand sample		Values
Median particle size, D_{50} (mm)		0.33
Specific gravity, G_s		2.65
Minimum dry density, $\rho_{d\min}$ (kg/m^3)		1420
Maximum dry density, $\rho_{d\max}$ (kg/m^3)		1710
(b) Measured from the modeled ground	Initial	After 5 d
Shear strength ($z' = 1.5, 7.5, 15$ cm), τ (kN/m^2)	0.4, 1.7, 2.5	2.5, 5.8, 9.4
Average settlement (cm)	-	1.4
Volume reduction, ΔV (%)	-	9.33
Dry density, ρ_d (kg/m^3)	1450	1600
Void ratio, e	0.823	0.656
Saturated unit weight, γ_s (kN/m^3)	18.68	19.58
Submerged unit weight, $\gamma' = \gamma_s - \gamma_w$ (kN/m^3)	8.87	9.77
Relative density, Dr (%)	13.5	66.8

(13.5%) and after 5 d (66.8%) classified the sand deposits as being in the "loose" and "medium-dense" compaction conditions, following the criteria proposed by Das and Sobhan (2014). Table 3.2 summarizes the sediment properties for D_{50} = 0.33 mm.

3.3 Calibrations Process

Before the instrumental setup, calibration equations were determined for the WGs, *CCM*, and PTs, as shown in Fig. 3.8. To compute water surface elevation (η), calibration of the wave gauge is required as it records the changes in water level in voltage (V). While maintaining a stable water surface, the wave gauge was gradually lowered by 5 cm at 1 cm intervals. At each 1 cm interval, the data (frequency: 50 Hz) was recorded using a data logger (*Model: midi LOGGER GL900, Graphtec Corporation*). The calibration results are visually presented in Fig. 3.8a.

For the *CCM*, the calibration process involved the preparation of a light-proof bucket, filling it with 10 L of water, and gradually adding 20 g of D_{50} = 0.33 mm silica sand while stirring with a mechanical stirrer. The pictorial view of this procedure is outlined in the Appendix (see Fig. A.6). The addition of each 20 g of sand in 10 L resulted in a 2 g/L increase in suspended sediment concentration. The cumulative sand weight reached 400 g (equivalent to 40 g/L). At each stage of adding 20 g of sand, the corresponding voltage (V) was recorded in the data logger (frequency: 50 Hz) for 20 s. The 20 s average of voltage was then plotted against the suspended sediment concentration (C), and this data was utilized to calculate the calibration equation, as illustrated in Fig. 3.8b.

To calibrate a pore pressure gauge (PTs), the transducers were affixed with L-shaped ruler at 2 cm intervals. The whole setup was again taped with elevator to maintain a horizontal alignment with the elevator. The measuring procedure included lowering the elevator at 1cm intervals. At each water depth, the data was recorded (frequency: 100 Hz) by a dynamic data acquisition software (DCS-100A) as the strain value. The details of the measuring procedure are presented in the Appendix (see Fig. A.7). Measurements were taken for approximately 10 s at each depth, and the average value was calculated and plotted against water level, as shown in Fig. 3.8c. The water level (h) was initially calculated from the recorded strain values

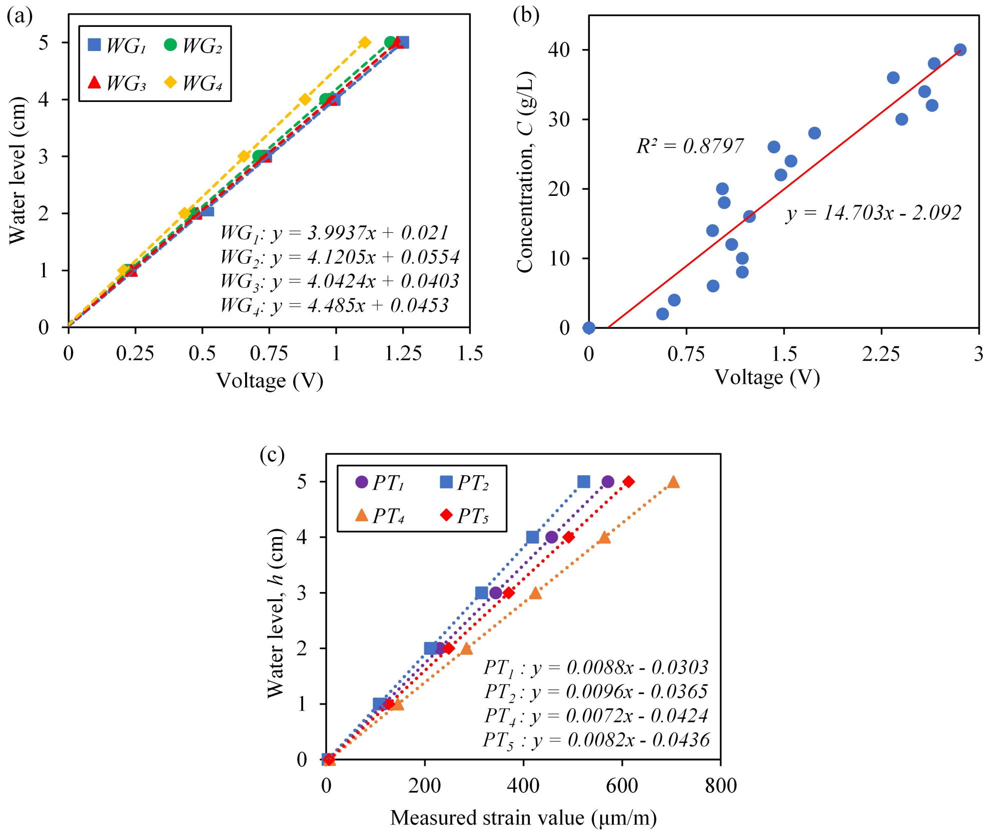

Figure 3.8: Calibration for (a) wave gauges (b) conductivity concentration meter, and (c) pressure transducers.

using the calibration equations. The pore pressure (p) was then calculated in kPa using Eq. 3.1, where h is the water level (cm), and g is the gravitational acceleration (m/s^2).

$$p = \frac{gh}{100} \tag{3.1}$$

3.4 Experimental Scenarios

A total of 16 experiments were conducted with the sandbar setup for a sediment size (D_{50}) of 0.33 mm and 0.08 mm under loose and medium-dense compaction conditions, as shown in Table 3.3. Before the wave action for each loose compaction condition (e.g., cases C1, C1a, C3, C5, C5a, C7, C7a, and C9), a water flow of 2.5 gpm (~ 0.15 L/s) was passed through the hose pipe for 5 min to achieve the loose compaction state of the sandbar. The sediment bed became loose due to the upward flow of water that reduced the shear strength (τ). The sandbar profile changed after completion of the wave action under loose compaction. The entire sandbar setup was left undisturbed for 5 d to achieve medium-dense compaction (M. Dense) conditions. A piston-type wavemaker was used to generate regular waves in absorption mode. The breaker-type in each case was identified based on the surf similarity parameter (ξ_0) proposed by Battjes (1974).

Table 3.3: Summary of hydrodynamic and sediment conditions

Cases	D_{50} (mm)	Compaction (τ_{mid}, kN/m^2)	H (m)	T (s)	H_0/L_0	Breaker-type (ξ_0)
C1	0.33	Loose (3.24)	0.10	1.0	0.081	Spilling (0.35)
C1a	0.08	Loose (1.08)	0.10	1.0	0.081	Spilling (0.35)
C2	0.33	M. Dense (5.12)	0.10	1.0	0.077	Spilling (0.36)
C2a	0.08	M. Dense (8.90)	0.10	1.0	0.077	Spilling (0.36)
C3	0.33	Loose (3.67)	0.10	1.8	0.032	Plunging (0.56)
C4	0.33	M. Dense (6.24)	0.10	1.8	0.031	Plunging (0.57)
C5	0.33	Loose (4.59)	0.10	1.4	0.041	Plunging (0.50)
C5a	0.08	Loose (3.46)	0.10	1.4	0.041	Plunging (0.50)
C6	0.33	M. Dense (6.92)	0.10	1.4	0.040	Plunging (0.50)
C6a	0.08	M. Dense (10.18)	0.10	1.4	0.040	Plunging (0.50)
C7	0.33	Loose (4.57)	0.08	1.8	0.024	Plunging (0.65)
C7a	0.08	Loose (3.56)	0.08	1.8	0.024	Plunging (0.65)
C8	0.33	M. Dense (7.76)	0.08	1.8	0.024	Plunging (0.65)
C8a	0.08	M. Dense (8.07)	0.08	1.8	0.024	Plunging (0.65)
C9	0.33	Loose (4.85)	0.08	1.0	0.062	Spilling (0.40)
C10	0.33	M. Dense (7.28)	0.08	1.0	0.063	Spilling (0.40)

3.5 Data Processing

3.5.1 Shear Strength Measurement

The maximum torque rotation was recorded using a torque meter (*FTD20CN-S, Tohnichi Mfg. Co. Ltd.*) at three different cross-shore locations (x = 150, 200, 250 cm) of sandbar, as shown in Fig.3.3b. The red dot in the figure indicates the location where the maximum torque rotation was measured. Additionally, to understand the variation in different layers of the sandbar, torque was recorded at three different depths (z') of 1.5, 7.5, and 15 cm from the top surface of the sandbar, as shown in Fig. 3.9.

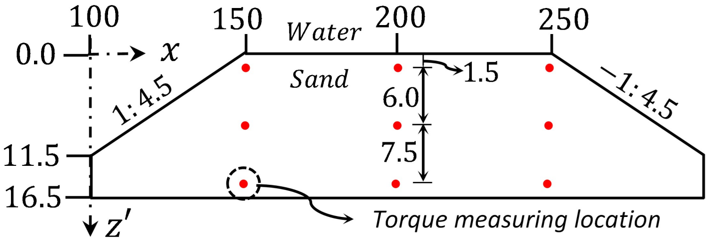

Figure 3.9: Torque measuring locations at different depths of sandbar.

Hence, shear strength (τ) in N/m^2 was calculated using Eq. (3.2), where M_{max} represents the maximum torque rotation (N-m), D is the vane width (m), and H is the vane height (m). After 10 min of wave action, the change in shear strength ($\Delta\tau$) was calculated by Eq. (3.3).

$$\tau = \frac{M_{\mathrm{max}}}{\pi\left(\frac{D^2H}{2} + \frac{D^3}{6}\right)} \tag{3.2}$$

$$\Delta\tau = \tau_{\mathrm{t=10}} - \tau_{\mathrm{t=0}} \tag{3.3}$$

3.5.2 Phase-averaged Analysis

To calculate the phase-averaged values of the pore pressure, water surface elevation, and sediment concentration, a Python library called SciPy was used (Virtanen et al., 2020). In this method, 10 consecutive periods are selected from the time-series data based on the zero-up-crossing method within a specific time interval (Fig. 3.10a). An overlapping procedure was then applied for 10 consecutive periods. During this process, the selected time intervals overlapped to ensure continuous analysis. Calculations were performed for each overlapping period to determine the standard deviations and phase-averaged values (Fig. 3.10b).

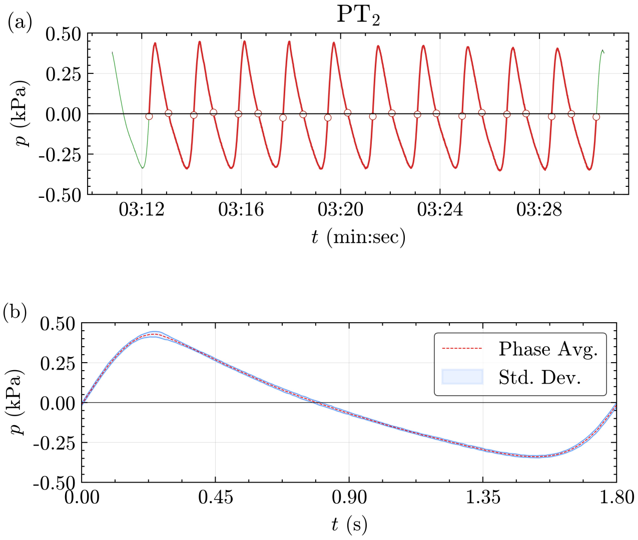

Figure 3.10: Phase-averaging of the pore pressure in case C7: (a) 10 consecutive wave periods based on zero-axis crossing; and (b) phase-averaged pore pressure values over the 10 periods.

3.5.3 Pore Pressure Gradients

Pore pressure (p) was calculated from the strain values recorded in the dataset. During the experiment, PT_3 and PT_6 did not provide reliable data because of instrumental malfunctions. These PTs were therefore, not considered when calculating the pore pressure gradient. The horizontal pore pressure gradient ($\partial p/\partial x$) was calculated using Eq. 3.4, where Δx represents the horizontal spacing (2 cm) between each PT. A positive $\partial p/\partial x$ is directed onshore.

$$\frac{\partial p}{\partial x} = \frac{p_1 - p_2}{\Delta x} \tag{3.4}$$

A third-order accurate pressure difference formula was approximated to calculate the vertical pore pressure gradient ($\partial p/\partial z$) at the level of PT_2 (see Eq. 3.5) similar to those described by Anderson et al. (2017); Suzuki et al. (2010). The Eq. (3.5) can be derived using Taylor expansion techniques for the first derivatives.

$$\frac{\partial p}{\partial z} = \frac{-3p_2 + 4p_4 - p_5}{2\Delta z} \tag{3.5}$$

Where Δz is the vertical spacing (2 cm) between each PT, and a positive $\partial p/\partial z$ is directed downward.

3.6 Repeatability of the Experiment

3.6.1 Morphological Repeatability

Before data recording, several trials were conducted to ensure the experiment's repeatability. In every experimental case, careful consideration was given to the sandbar's ground conditions during the sand filling procedure. The same falling height and compaction conditions were maintained to ensure consistency. Fig. 3.11 illustrates the morphological repeatability of case C3 and case C3 (repeat), where the wave height (H) was 10 cm and the wave period (T) was 1.8 s. The corresponding volume change (ΔV) is also plotted for better understanding. From the sandbar's bed-level changes at different recording times (e.g., t = 10, 20, and 30 min), it is clear that a consistent volume change was observed in both cases. This consistency confirms the reproducibility of the experimental setup and the reliability of the observed results.

3.6.2 Repeatability in Shear Strength

Furthermore, the detailed shear strength scenario for the sandbar is provided in Fig. 3.12. To ensure similar initial ground conditions for each case, the maximum torque rotation was carefully recorded at three cross-shore locations of the sandbar (x = 150, 200, and 250 cm) and three distinct sandbar layers (z' = 1.5, 7.5, and 15 cm) at the beginning of wave action and after 10 min of wave action. An average of 9 measuring locations is represented by

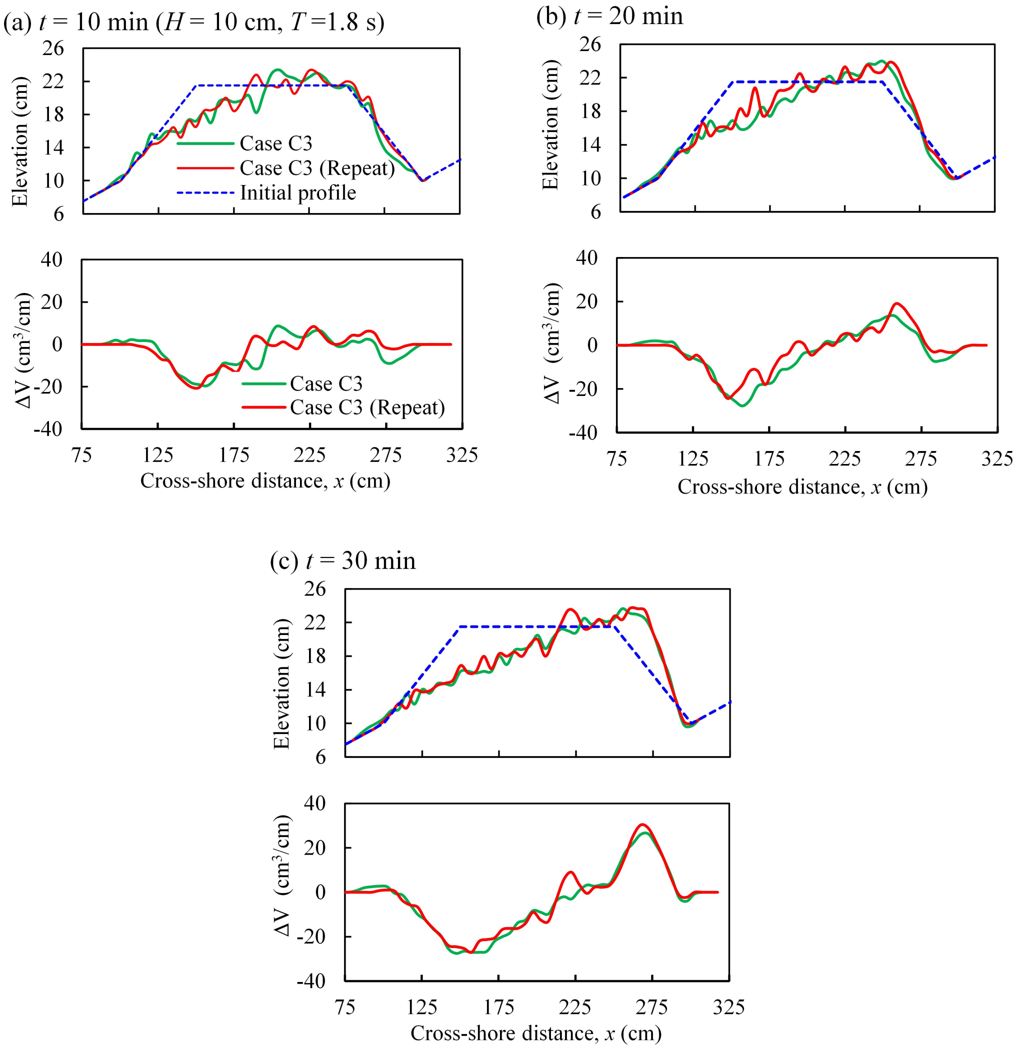

Figure 3.11: Repeatability of morphology change for case C3 and C3 (repeat). Sub-figures (a), (b), and (c) show the morphology change in every 10 min, and their corresponding volume change (ΔV).

each data point. The green line indicates the standard deviations of the data points. From the figure, it is clear that the shear strength in the top layer is almost similar for both case C3 and C3 (repeat). Since the top and middle layers were primarily implicated in erosion and the maximum depth of the pressure transducers (PT_s) was located at $z' = 7$ cm from the top surface of the sandbar, efforts were made to maintain similar shear strength up to the middle layer of the sandbar ($z' = 7.5$ cm). However, the slightly higher shear strength identified in the repeated conditions for the bottom layer, located at $z' = 15$ cm, was considered negligible in the experiment.

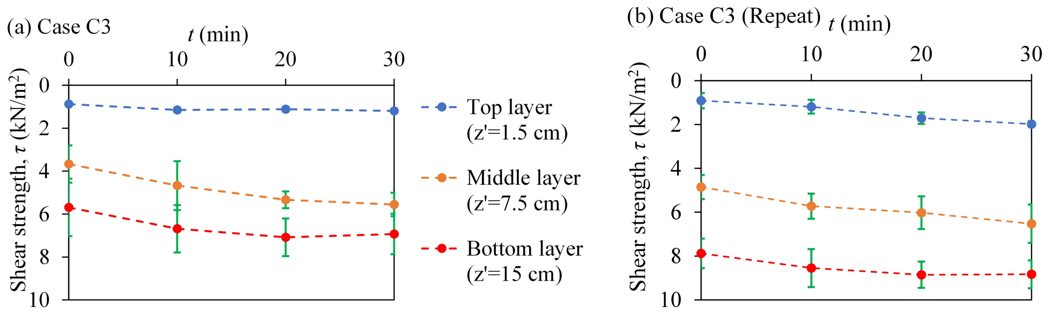

Figure 3.12: Temporal variation of shear strength at different depths of sandbar for case (a) C3 and (b) C3 (repeat).

Chapter 4

Effect of Sediment Size on Sandbar Morphology

The following text in this chapter interpolates the results and discussions from Islam and Suzuki (2023), the author's published article titled *Effect of Sediment Size on Sandbar Morphology in Different Compaction Conditions*. By integrating these findings, this chapter aims to provide a comprehensive analysis of how variations in sediment size influence sandbar morphology and shear strength within the broader experimental framework. In this chapter, the impact of two distinct sediment sizes (D_{50} = 0.33 mm and 0.08 mm) on sandbar morphology is examined. Additionally, an analysis of change in shear strength corresponding to different wave steepness is presented. To comprehend the influence of sediment size, six distinct cases are selected with varying wave steepness (H_0/L_0) from the D_{50} = 0.33 mm datasets. These cases include scenarios of low (cases C7 and C8), medium (cases C5 and C6), and high (cases C1 and C2) wave steepness. Similarly, corresponding cases are chosen from the D_{50} = 0.08 mm datasets, ensuring consistency in wave conditions. These cases encompass scenarios of low (cases C7a and C8a), medium (cases C5a and C6a), and high (cases C1a and C2a) wave steepness.

4.1 Morphological Evolution of the Sandbar

Fig. 4.1 illustrates the evolution of sandbar profiles and the corresponding volume change (ΔV) at various cross-shore locations for cases C5 and C5a (H = 10 cm, T = 1.4 s), as well as C7 and C7a (H = 8 cm, T = 1.8 s), all under loose compaction conditions. To assess sandbar erosion and accretion, the initial profile of the sandbar under loose conditions was modeled as a trapezoidal shape, delineated by the green dashed line in Figs. 4.1a and c. During the wave action, the variation in bed-level of sandbar was recorded. The impinging zones for cases C5 and C5a were x = 205 to 220 cm, and cases C7 and C7a were x = 245 to 275 cm, respectively, as denoted by the shaded areas in the figure.

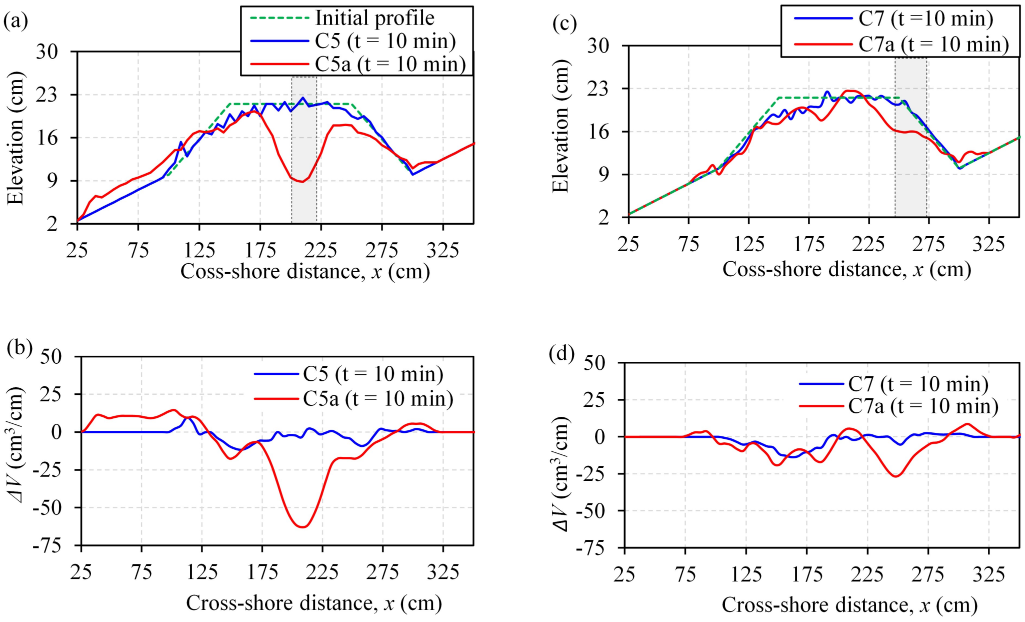

Figure 4.1: Example of sandbar profile evolution and corresponding volume change (ΔV) under loose compaction. Cases C5 and C7 correspond to D_{50} = 0.33 mm, while cases C5a and C7a correspond to D_{50} = 0.08 mm.

The experimental results revealed that the sandbar migrated onshore with their shapes dissipating gradually by the formation of rippling throughout the profiles under loose compaction conditions considering D_{50} = 0.33 mm (Fig. 4.1a, Blue line), which was also observed by Li et al. (2022). There was no significant erosion at the impinging zone in the mechanism of wave breaking in case of D_{50} = 0.33 mm sandbar. In case C5, the maximum local erosion and accretion volume were 11.75 cm^3/cm and 9.5 cm^3/cm at x = 155 cm and x = 110 cm, respectively, as shown in Fig. 4.1b. Similarly, the maximum local erosion volume for cases C1 and C7 was 6.0 cm^3/cm (x = 225 cm) and 13.75 cm^3/cm (x = 160 cm), respectively. Conversely, in the loose compaction conditions of D_{50} = 0.08 mm sandbar (Fig. 4.1a, Red line), significant erosion occurred at an impinging zone during the wave action. In case of C5a, the maximum local erosion volume was 63 cm^3/cm at the impinging point (x = 210 cm) due to a plunging-type wave breaker. Similarly, the maximum local erosion volume was 20.75 cm^3/cm and 26.75 cm^3/cm for cases C1a and C7a, respectively. The effect of plunging-type wave breaking was the possible reason for over-wash deposits (14.5 cm^3/cm) on the offshore edge of the sandbar (x = 105 cm) in this case (C5a). In case of C1a, a significant deposition volume (41.25 cm^3/cm) was found on the onshore side (x = 305 cm) due to the spilling type of wave breaking.

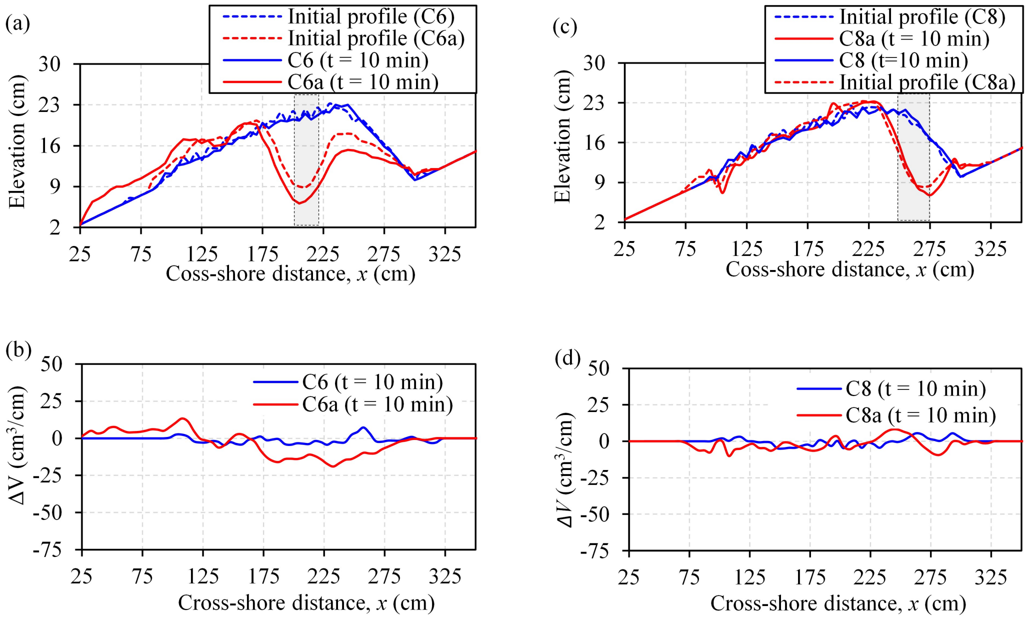

Figure 4.2: Illustration of sandbar profile changes and volume change (ΔV) under medium-dense compaction. Cases C6 and C8 represent D_{50} = 0.33 mm, while cases C6a and C8a represent D_{50} = 0.08 mm.

Fig. 4.2 depicts the changes in sandbar profiles and the associated volume change (ΔV) under medium-dense compaction conditions for cases C6 and C6a (H = 10 cm, T = 1.4 s), as well as C8 and C8a (H = 8 cm, T = 1.8 s). The initial sandbar profile is represented by the blue dashed line for D_{50} = 0.33 mm sandbar (cases C6 and C8) and the red dashed line for D_{50} = 0.08 mm sandbar (cases C6a and C8a). The area of wave breaking in the impinging zone was observed between x = 205 to 220 cm for case C6 and C6a, and between x = 245 to 275 cm for case C8 and C8a, respectively, as indicated by the shaded area in Figs. 4.2a and c. Due to the compacted sandbar, the erosion volume decreased under medium-dense compaction conditions compared to loose compaction with the same sediment size. In case of C6, the maximum local erosion volume was 4.5 cm^3/cm at x = 145 cm, while the maximum local accretion volume was 7.25 cm^3/cm at x = 260 cm. The erosion volume also significantly reduced in case C8, as shown in Fig. 4.2c. For the D_{50} = 0.08 mm sandbar, both erosion and accretion volumes decreased under medium-dense conditions. For instance, in case of C6a, the maximum local erosion volume was reduced to 19 cm^3/cm at x = 235 cm.

4.2 Maximum Local Erosion Depth

Fig. 4.3 represents the variation of maximum local erosion depth in different cross-shore locations. Considering all cases of loose compaction conditions of D_{50} = 0.33 mm, the maximum erosion zone was located at the offshore sharp end of the sandbar (x = 150 cm to 160 cm). The highest value of the maximum local erosion depth was 3 cm at x = 160 cm in case C7. Conversely, under loose compaction conditions with D_{50} = 0.08 mm, the highest maximum local erosion depth was 12.7 cm at the impinging point (x = 210 cm) in case C5a, caused by plunging wave breaking. Overall, the maximum local erosion depth increased significantly, averaging 3.2 times greater than that observed with D_{50} = 0.33 mm.

In context of medium-dense compaction with D_{50} = 0.33 mm, the highest value of maximum local erosion depth was reduced to 1.9 cm in case C2 (Fig. 4.3b). Also, the location of this highest value slightly moved towards the middle ($x = 175$ cm) of the sandbar. On the other hand, under medium-dense compaction conditions of $D_{50} = 0.08$ mm, the highest value of maximum local erosion depth significantly decreased (around 70%) to 3.9 cm at $x = 230$ cm in case C6a.

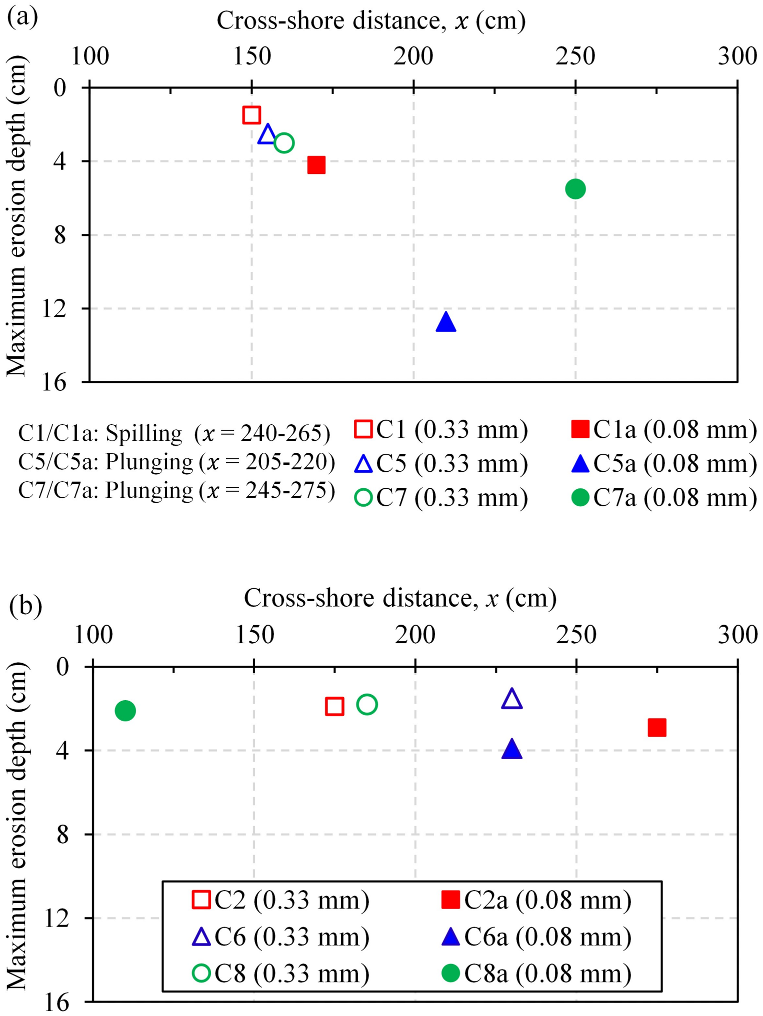

Figure 4.3: Variation of maximum local erosion depth in different cross-shore locations for (a) loose and (b) medium-dense compaction conditions.

4.3 Sandbar Erosion Volume with Wave Steepness

In order to compute the net erosion volume (ΔV_e), the sandbar volume at $t = 10$ min was deducted from the initial sandbar volume, within the range of $x = 100$ cm to $x = 300$ cm. As studies have shown that wave steepness (H_0/L_0) contributes considerably to sandbar erosion volume, H_0/L_0 was taken into account with net erosion volume (Demirci et al., 2014). Fig. 4.4 depicts the relationship between net erosion volume of sandbar and H_0/L_0.

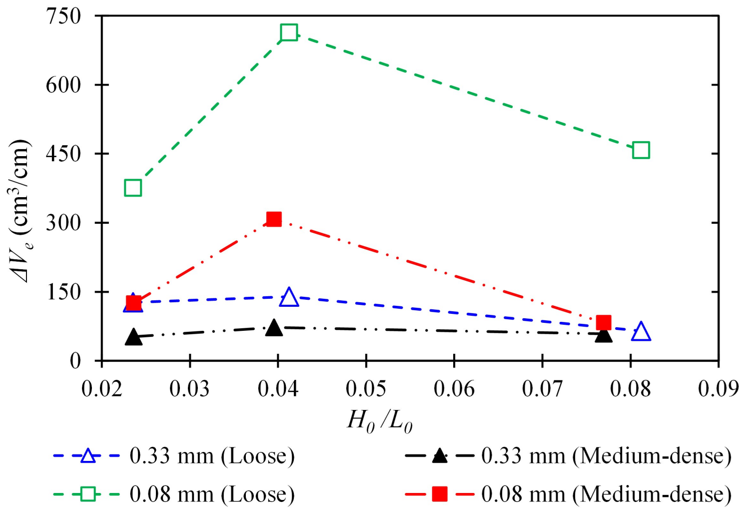

Figure 4.4: Correlation between net erosion volume and wave steepness.

In loose compaction conditions with $D_{50} = 0.33$ mm (blue dashed line), the low H_0/L_0 (0.024) and medium H_0/L_0 (0.041) resulted in nearly the same higher net erosion volume due to the plunging type of wave breaking, whereas the high H_0/L_0 (0.081) revealed a lower net erosion volume due to the spilling type wave breaking. A strong inverse correlation ($R^2 = 0.80$) was established with increasing H_0/L_0. Conversely, a nearly similar net erosion volume was found in different H_0/L_0 under medium-dense compaction conditions (black dashed line).

With loose compaction conditions with $D_{50} = 0.08$ mm (green dashed line), the net erosion volume increased, reaching a sharp peak at the medium H_0/L_0, and then decreasing at the high H_0/L_0. The plunging type of wave breaking with a high wave height ($H = 10$ cm) in a 13.5 cm water column above sandbar may be responsible for the sharp peak observed at the medium H_0/L_0. On the other hand, a significant reduction in net erosion volume was observed under medium-dense compaction conditions of the same sediment. For instance, the reduction of net erosion volume was 67%, 57%, and 82% at low, medium, and high H_0/L_0, respectively in medium-dense conditions. Hence, it was difficult to figure out any linear correlation of net erosion volume with increasing H_0/L_0.

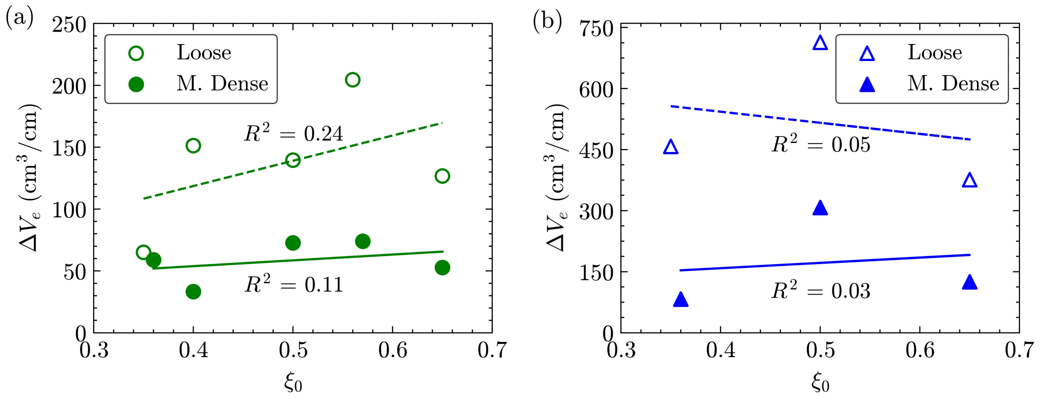

Figure 4.5: Scatterplot of net erosion volume (ΔV_e) with surf similarity parameters (ξ_0) for (a) $D_{50} = 0.33$ mm and (b) $D_{50} = 0.08$ mm.

Fig. 4.5 shows the sandbar net erosion volume (ΔV_e) in relation to the surf similarity parameter (ξ_0) for sandbars with $D_{50} = 0.33$ mm and 0.08 mm. According to Battjes (1974), a value of $\xi_0 < 0.5$ indicates a spilling-type of breaking wave, while a higher value correspond to a plunging-type of breaking wave. In Fig. 4.5a, under loose compaction conditions, the spilling-type of breaking wave ($\xi_0 = 0.35$) exhibited the smallest erosion volume. Despite both cases involving spilling-type of breaking, a significantly higher erosion volume was observed in loose compaction when ξ_0 increased to 0.40. In this cases, a weak correlation ($R^2 = 0.24$) was established between sandbar erosion volume and surf similarity parameter ξ_0. Conversely, for the $D_{50} = 0.33$ mm sandbar under medium-dense compaction, the erosion volume remained almost similar, regardless of the breaking wave-type, due to the uniformly compacted sandbar conditions. Overall, a weak correlation

($R^2 = 0.11$) was observed in this regard.

In the context of sandbar with $D_{50} = 0.08$ mm (Fig. 4.5b), there was an increasing trend in erosion volume up to a specific value of breaker type (e.g., $\xi_0 = 0.5$), followed by a decrease with further increases in the value of ξ_0. A similar increasing trend of average sediment concentration was also found in the same case (cases C5a and C6a; $H_0/L_0 = 0.041$), as shown in in the next chapter (Fig. 5.11). It is very hard to identify any correlation between the erosion volume and surf similarity parameters.

4.4 Shear Strength under Varying Compaction

Fig. 4.6 shows the variation of shear strength at the three cross-shore locations under loose compaction conditions for $D_{50} = 0.33$ mm and 0.08 mm: the offshore edge of the sandbar ($x = 150$ cm), the middle of the sandbar ($x = 200$ cm), and the onshore edge of the sandbar ($x = 250$ cm). For $D_{50} = 0.33$ mm, the initial shear strength in the top layer ($z' = 1.5$ cm) of the sandbar was almost the same in cases C5 and C7. However, in the middle ($z' = 7.5$ cm) and bottom ($z' = 15$ cm) layers, the initial shear strength was approximately 40% higher due to the retention of the compaction state from the previous wave action. At the middle of the sandbar ($x = 200$ cm), after 10 min of wave action, the shear strength at the bottom layer was 6.09 kN/m^2 for case C1, 8.33 kN/m^2 for case C5, and 8.98 kN/m^2 for case C7.

Conversely, significant variation in initial shear strength was observed at the offshore edge ($x = 150$ cm) and the middle ($x = 200$ cm) of the sandbar for $D_{50} = 0.08$ mm, as shown in Figs. 4.6d and f. In Fig. 4.6e, the shear strength values were not found in the top and middle layers of case C5a due to significant erosion at $x = 200$ cm, as described in Fig. 4.1. In all cases for $D_{50} = 0.08$ mm, the shear strength at $t = 10$ min was significantly higher than for $D_{50} = 0.33$ mm. For instance, at $x = 200$ cm, after 10 min of wave action, the shear strength for the bottom layer was 9.49 kN/m^2 for case C1a, 13.75 kN/m^2 for case C5a, and 10.62 kN/m^2 for case C7a.

Fig. 4.7 illustrates the variation in shear strength at three different cross-shore locations under medium-dense compaction conditions for $D_{50} = 0.33$ mm and $D_{50} = 0.08$ mm. Significant variations in initial shear strength

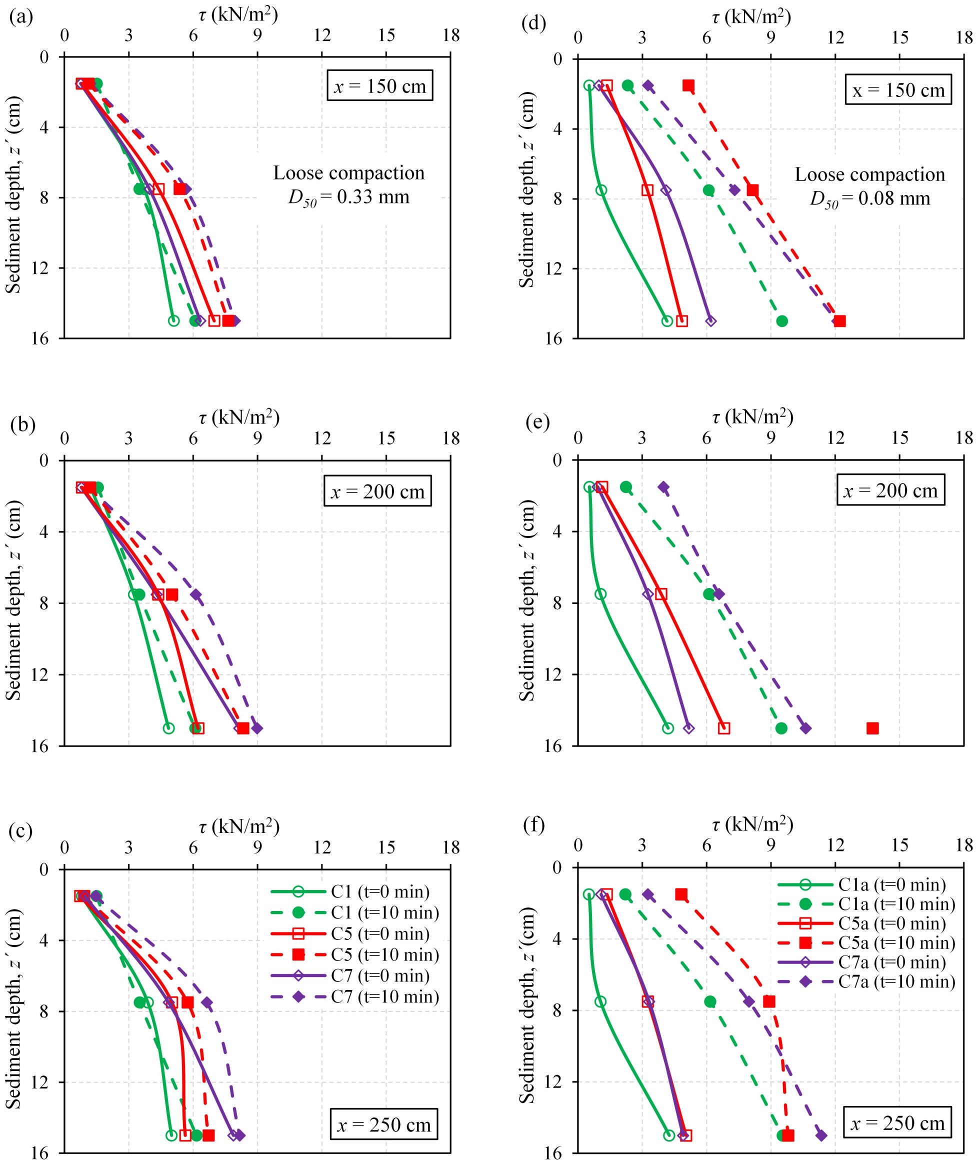

Figure 4.6: Variation of shear strength at different cross-shore locations under loose compaction. Sub-figures a, b, and c represent D_{50} = 0.33 mm, while sub-figures d, e, and f correspond to D_{50} = 0.08 mm.

were observed in all cases due to wave loading under loose compaction conditions. For D_{50} = 0.33 mm, the medium-dense compaction resulted in a slight increase in shear strength (see Figs. 4.7a, b, and c). On the other hand, the sandbar with D_{50} = 0.08 mm sediment exhibited high shear strength after 10 min of wave action, even though its initial shear strength was higher than that of the D_{50} = 0.33 mm sandbar (Figs. 4.7d, e, and f).

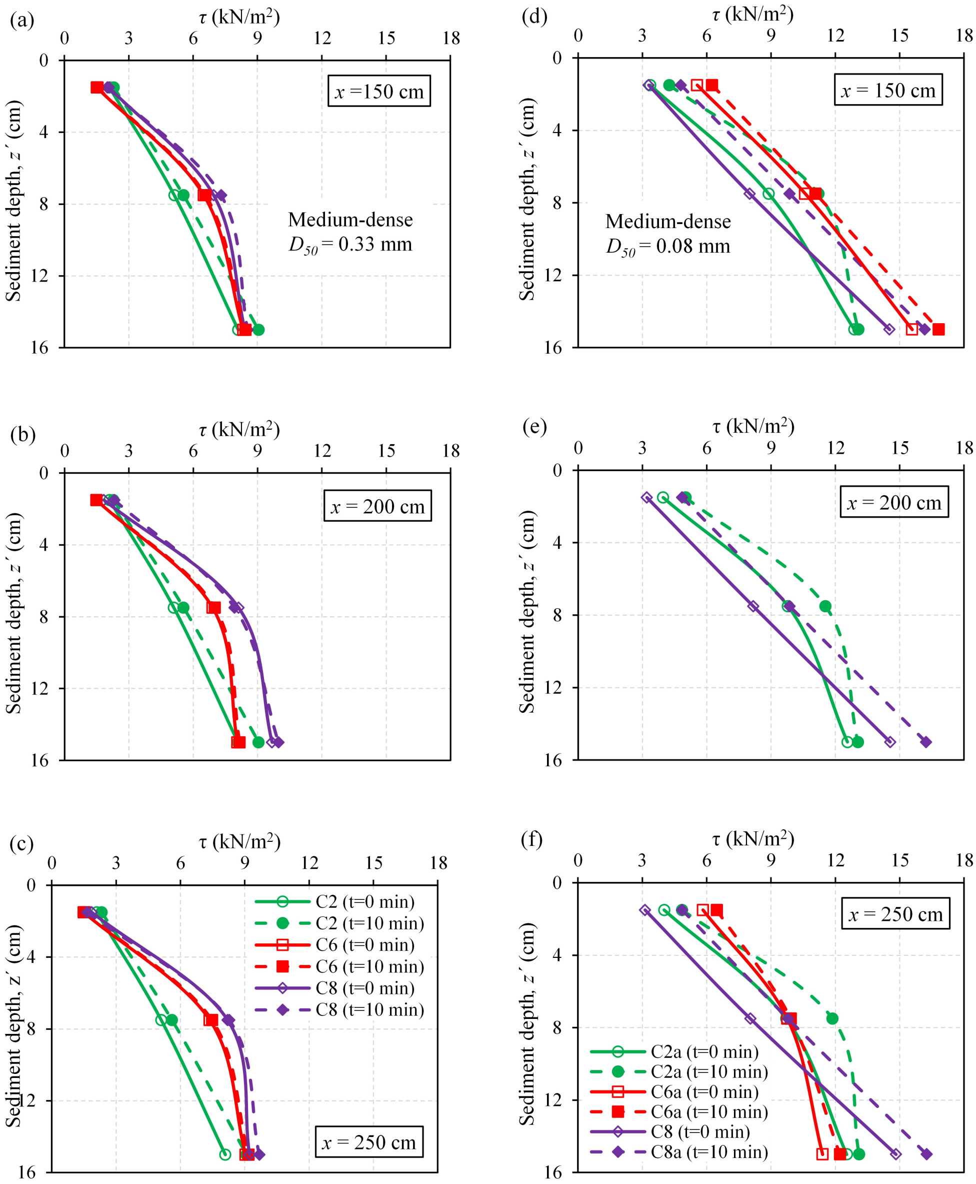

Figure 4.7: Variation of shear strength at different cross-shore locations under medium-dense compaction. Sub-figures a, b, and c represent D_{50} = 0.33 mm, while sub-figures d, e, and f correspond to D_{50} = 0.08 mm.

4.5 Change in Shear Strength and Wave Steepness

Fig. 4.8 shows the variation of change in average shear strength ($\Delta\tau_{\text{avg}}$) with H_0/L_0 at loose compaction conditions. First, the change in shear strength ($\Delta\tau$) of each section (e.g., $x = 150$ cm) was calculated by Eq. (3.3). Then, $\Delta\tau_{\text{avg}}$ was calculated by a simple average at $x = 150$ cm, 200 cm, and 250 cm. Furthermore, a linear regression analysis was used to know the physical significance of $\Delta\tau_{\text{avg}}$ with H_0/L_0.

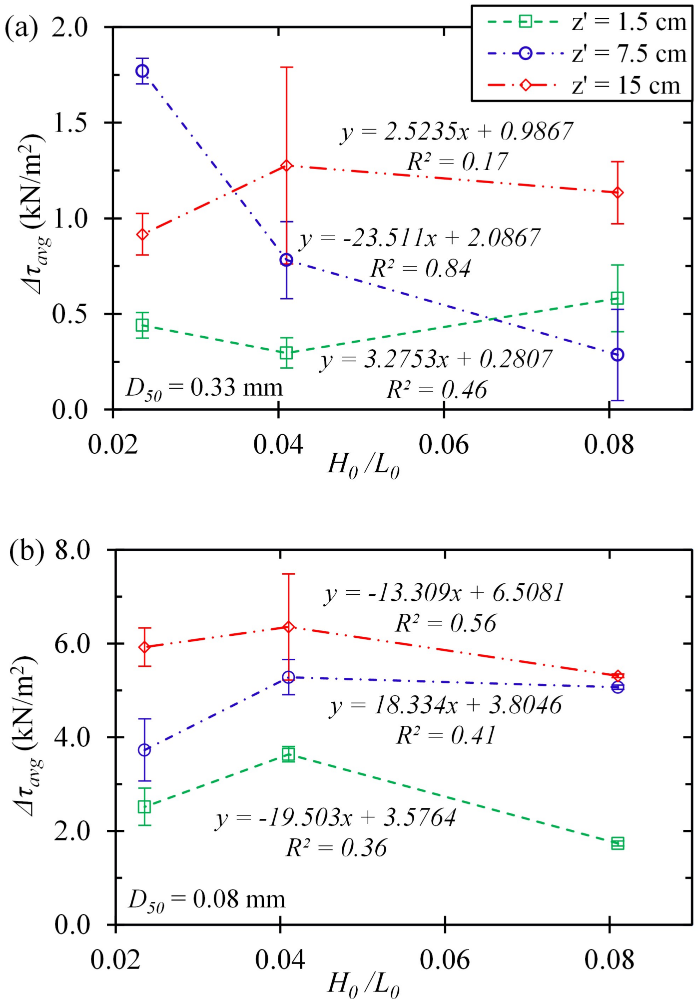

Figure 4.8: Variation of change in shear strength with wave steepness in loose compaction conditions for (a) $D_{50} = 0.33$ mm and (b) $D_{50} = 0.08$ mm.

In loose compaction of D_{50} = 0.33 mm (Fig. 4.8a), the highest and lowest $\Delta\tau_{\text{avg}}$ were 1.77 kN/m^2 and 0.29 kN/m^2 at the middle layer of the sandbar in the low H_0/L_0 (0.024) and high H_0/L_0 (0.081), respectively. At the top layer, the magnitude of $\Delta\tau_{\text{avg}}$ was very low due to the excessive wave-sediment interaction under different H_0/L_0. A weak positive correlation (R^2 = 0.46) was obtained between $\Delta\tau_{\text{avg}}$ and H_0/L_0 at this layer. Conversely, at the middle layer, dynamic wave-sediment interaction as well as the considerable effect of the constant wave loading resulted in significant variations of $\Delta\tau_{\text{avg}}$ under different H_0/L_0. A strong inverse correlation (R^2 = 0.84) between $\Delta\tau_{\text{avg}}$ and H_0/L_0 was found at this layer. At the bottom layer, the effect of constant wave loading resulted in high $\Delta\tau_{\text{avg}}$ although there was very low wave-sediment interaction. At this layer, it was hard to find any correlation.

In loose compaction considering D_{50} = 0.08 mm (Fig. 4.8b), the highest and lowest $\Delta\tau_{\text{avg}}$ were observed at the bottom and top layers, respectively. A sharp peak of $\Delta\tau_{\text{avg}}$ was obtained at medium H_0/L_0, which was also reflected in net erosion volume, as mentioned in Fig. 4.4. Although plunging-type wave breaking was observed in both the low H_0/L_0 and medium H_0/L_0, however, the corresponding wave height at medium H_0/L_0 was 2 cm higher than low H_0/L_0 (Table 3.3). Also, a significant effect of an impinging point was found in all cases of D_{50} = 0.08 mm. Therefore, plunging-type wave breaking, and the effect of impinging point resulted in a sharp peak at medium H_0/L_0. Between $\Delta\tau_{\text{avg}}$ and H_0/L_0, a weak inverse correlation was found at the top layer. The middle layer revealed a weak correlation. Also, a moderate inverse correlation was observed at the bottom layer.

Table 4.1 represents the summary of correlation equations in medium-dense compaction conditions. For D_{50} = 0.33 mm, the middle layer of the sandbar followed the reverse trend of correlation (R^2 = 0.69) compared to the loose compaction conditions. A strong correlation (R^2 = 0.77) was obtained at the bottom layer, and the trend was similar to the loose compaction conditions. For D_{50} = 0.08 mm, a strong inverse correlation (R^2 = 0.75) existed at the bottom layer; however, it was hard to find any correlation at the top and middle layers. A possible reason for this was a large difference in the initial shear strength between medium H_0/L_0 (case C6a) and low H_0/L_0 (case C8a) at the top layer (Table 3.3).

Table 4.1: Correlation equations for shear strength at different depths

Depth, z' (cm)	Correlation equations	
	$D_{50} = 0.33$ mm	$D_{50} = 0.08$ mm
1.5	$y = -0.143x + 0.168$ $R^2 = 0.001$	$y = -8.652x + 1.407$ $R^2 = 0.16$
7.5	$y = 5.652x - 0.011$ $R^2 = 0.69$	$y = 13.565x + 0.716$ $R^2 = 0.14$
15	$y = 14.465x - 0.2196$ $R^2 = 0.77$	$y = -19.457x + 1.807$ $R^2 = 0.75$

Fig. 4.9 represents the correlation between percent volume reduction ($\Delta V_{\text{reduction}}$) and percent change in average in shear strength ($\Delta\tau_{\text{avg}}$). In the case of loose compaction conditions of sandbar with $D_{50} = 0.33$ mm, a strong correlation ($R^2 = 0.885$) was obtained between $\Delta V_{\text{reduction}}$ and $\Delta\tau_{\text{avg}}$. However, a weak correlation ($R^2 = 0.362$) existed in medium-dense compaction of the same sediment. Conversely, a good negative correlation ($R^2 = 0.708$ for loose compaction; $R^2 = 0.805$ for medium-dense compaction) was existed between $\Delta V_{\text{reduction}}$ and $\Delta\tau_{\text{avg}}$ of sandbar with $D_{50} = 0.08$ mm.

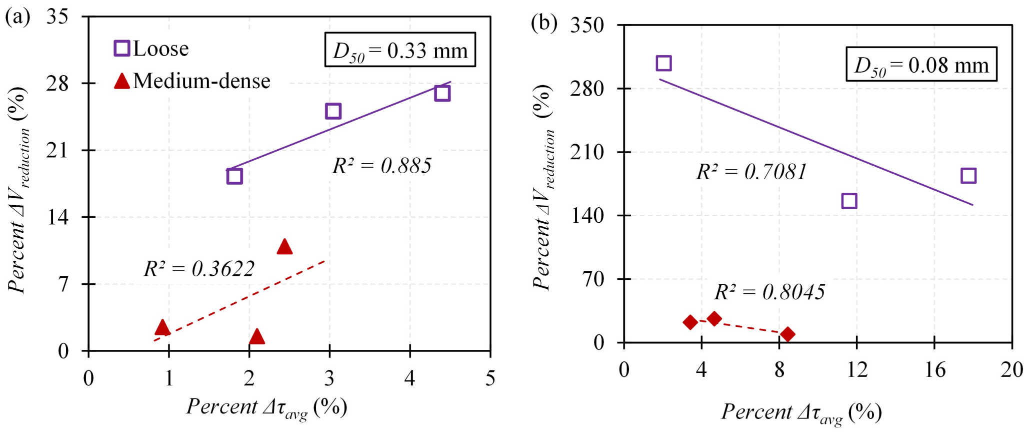

Figure 4.9: Correlation between percent volume reduction and change in average shear strength for (a) $D_{50} = 0.33$ mm and (b) $D_{50} = 0.08$ mm.

4.6 Summary of the Findings

This chapter aims to provide an in-depth analysis of how changes in sediment size affect sandbar morphology and shear strength under different compaction conditions within the broader context of the experimental framework. The summary of the findings is listed below:

1. For medium sand (D_{50} = 0.33 mm), the sandbar moved onshore, creating ripples along its profile. In contrast, very fine sand (D_{50} = 0.08 mm) experienced significant erosion, averaging 3.7 times more at the impinging zone.

2. For medium sand, the maximum erosion depth occurred at the offshore end of the sandbar, while for very fine sand, it was observed at the impinging zone.

3. Very fine sand exhibited a significantly higher net erosion volume compared to medium sand, averaging 3.7 times more in loose compaction and 1.8 times more in medium-dense compaction. For medium sand in loose compaction, there was a strong inverse correlation (R^2 = 0.80) between net erosion volume and wave steepness. Conversely, for very fine sand, a sharp peak was observed at medium wave steepness.

4. In loose compaction, the shear strength of very fine sand during the same wave action period was five times higher than that of medium sand at the middle layer of sandbar. At this layer, a strong inverse correlation (R^2 = 0.84) was established between the change in average shear strength and wave steepness under loose compaction conditions of medium sand, whereas a moderate correlation (R^2 = 0.69) was obtained under medium-dense compaction. Similar to net erosion volume, a sharp peak in shear strength was noted at medium wave steepness under loose compaction of very fine sand. In medium-dense compaction, a strong inverse correlation (R^2 = 0.75) was identified at the bottom layer, although no significant correlation was found for very fine sand at the top and middle layers of sandbar.

5. Regarding the correlation between percent volume reduction and the change in average shear strength for medium sand, a strong positive correlation ($R^2 = 0.885$) was observed under loose compaction conditions, while a similar trend with weaker correlation was observed under medium-dense compaction conditions. In contrast, a strong negative correlation ($R^2 = 0.708$ for loose compaction; $R^2 = 0.805$ for medium-dense compaction) was identified in the case of very fine sand.

Chapter 5

Dynamic Correlations: Pressure Gradients, Concentration, and Bed-level Erosion

The content in this chapter is derived from the results and discussions sections of the author's published articles, e.g., Islam et al. (2024), and Islam and Suzuki (2024). It is organized into four main sections. Section 5.1 delineates the responses of pore pressure under loose and medium-dense compaction conditions. Moreover, section 5.2 focuses quantification of liquefaction parameters (e.g., liquefaction index and liquefaction thickness) based on the maximum pore pressure responses. Section 5.3 focuses on the effect of wave steepness, sediment size, and sediment compaction on the sediment concentration. In section 5.4, the inter-correlations among the key parameters (e.g., pressure gradient, sediment concentration, and erosion volume) are presented. These discussions continue by exploring the dynamic correlation between the maximum phase-averaged vertical pressure gradient and the sediment concentration with the aim of understanding the temporal variation of these parameters. For explaining these parameters, cases C7 and C8 are selected as an example case throughout section 5.1 and 5.3. Also, four time-steps (e.g., t = 1.5, 3.5, 5.5, and 7.5 min) are selected for phase-average analysis.

5.1 Pore Pressure Responses

This section analyzes the phase-averaged pore pressure under loose and medium-dense compaction conditions for a sandbar with $D_{50} = 0.33$ mm. It presents the variations in both horizontal and vertical pore pressure gradients, and describes the attenuation of amplitude along with its corresponding phase lag.

5.1.1 Phase-Averaged Pore Pressure

Fig. 5.1 shows the effect of the water surface elevation (η) on the phase-averaged pore pressure (p) measured by the horizontal (PT_1 and PT_2) and vertical (PT_2, PT_4, and PT_5) pressure transducer array under loose (case C7) and medium-dense (case C8) compaction conditions at $t = 3.5$ min. The expression p/γ_w was used, ensuring unit consistency with η, where γ_w represents the unit weight of water ($\gamma_w = 9.8$ kN/m^3).

The pore pressure fluctuates with the generation of regular waves. The amplitude variation of the phase-averaged pore pressure of PT_1 and PT_2 (horizontal) showed little difference as the pressure transducers (PTs) were positioned at the same depth ($z' = 1.5$ cm). However, the loose compaction condition (Fig. 5.1b) showed relatively higher amplitude of p/γ_w than the medium-dense compaction condition (Fig. 5.1e), even though the observation depth of the transducers was the same. In the array of vertical transducers, the highest amplitude of p/γ_w was found at PT_2, while the lowest was recorded at PT_5 (Figs. 5.1c and f). In addition, a significant amplitude reduction was observed with increasing sediment depth under both loose and medium-dense compaction conditions. Under loose compaction (case C7), the maximum amplitudes of the phase-averaged pore pressures (p) at PT_2, PT_4, and PT_5 were 0.4277, 0.3453, and 0.326 kPa, respectively. Under medium-dense compaction conditions (case C8), the p values at PT_2, PT_4, and PT_5 were 0.3943, 0.3462, and 0.3299 kPa, respectively.

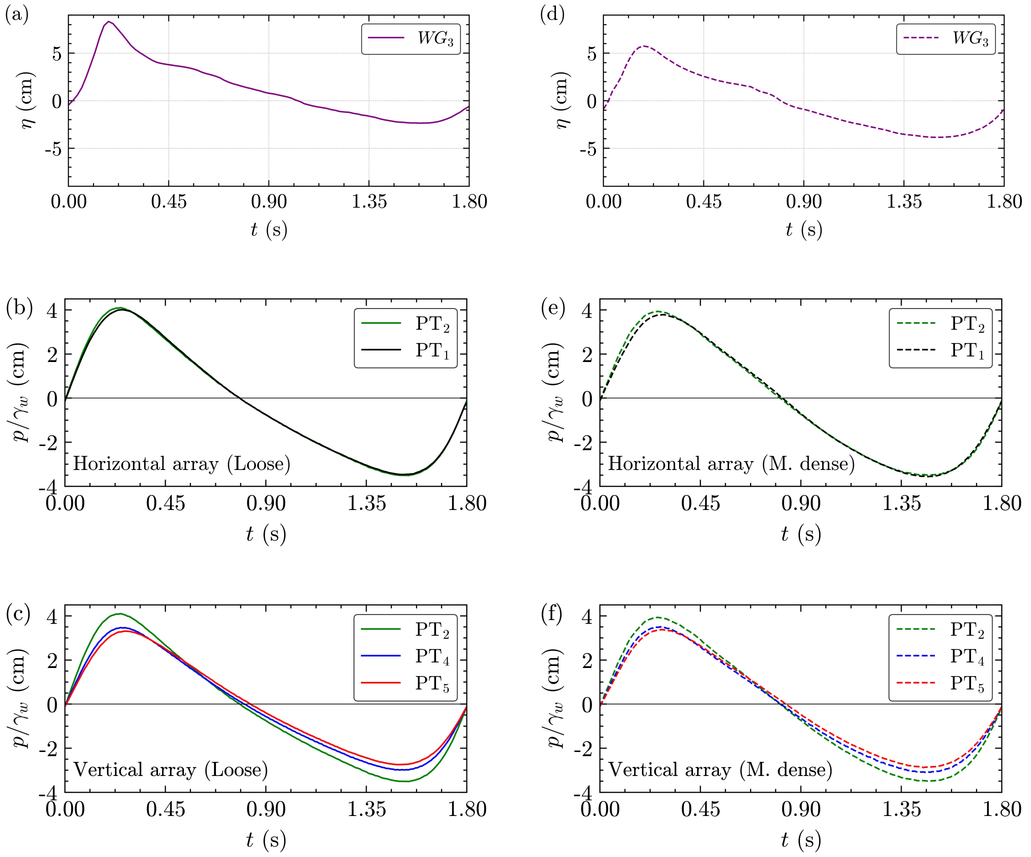

Figure 5.1: Phase-averaged pore pressure of horizontal (b) and (e), and vertical (c) and (d) *PT* arrays with water surface elevation (η) for wave steepness of 0.024: (a), (b), and (c) are for loose compaction (case C7); and (d), (e), and (f) are for medium-dense compaction (case C8).

5.1.2 Horizontal and Vertical Pore Pressure Gradients

Fig. 5.2 shows the horizontal and vertical pore pressure gradients under loose (case C7) and medium-dense (case C8) compaction conditions. The horizontal pore pressure gradient ($\partial p/\partial x$) was calculated using Eq. 3.4. The direction of the horizontal pore pressure gradient was offshore beneath the wave crest owing to its negative amplitude, whereas it was directed onshore beneath the wave trough under both compaction conditions, as shown in Figs. 5.2a and c. Although the wave conditions were similar in experimental cases C7 and C8, the amplitude of the horizontal pore pressure gradient under loose compaction conditions was higher than that under medium-dense compaction conditions.

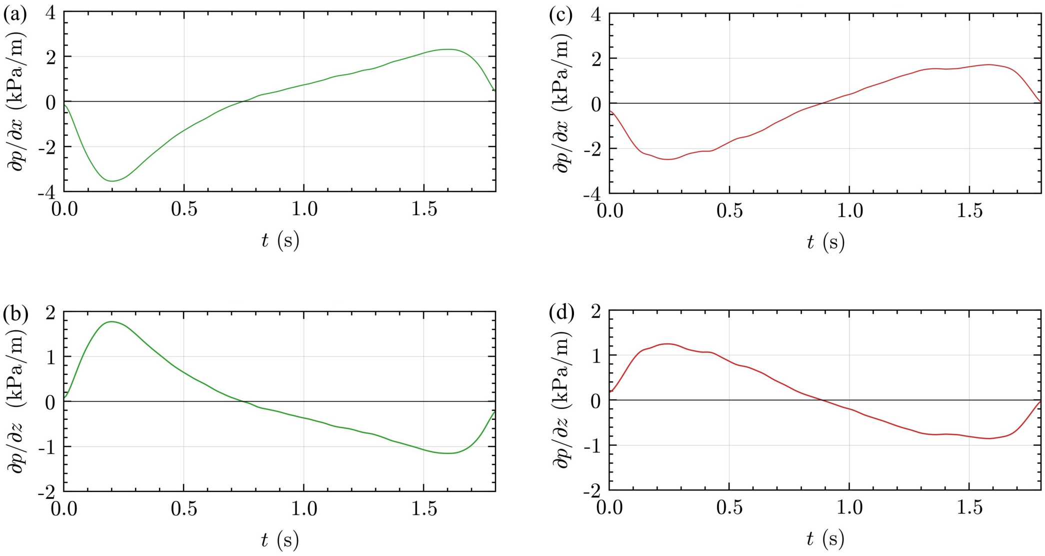

Figure 5.2: Horizontal ($\partial p/\partial x$) and vertical ($\partial p/\partial z$) pore pressure gradients: (a) and (b) under loose (case C7) compaction conditions; (c) and (d) under medium-dense (case C8) compaction conditions.

The vertical pore pressure gradient ($\partial p/\partial z$) was determined using the third-order accurate pressure difference formula outlined in Eq. 3.5. When the wave crest passed above the vertical PT array, the water pressure reached its peak, leading to a positive $\partial p/\partial z$, as shown in Figs. 5.2b and d. This positive value of $\partial p/\partial z$ shows the downward-directed vertical pore pressure gradient inside the sediment bed. In contrast, decreasing the water pressure beneath the corresponding wave trough resulted in a negative $\partial p/\partial z$, indicating an upward-directed vertical pore pressure gradient. A significant variation in the amplitude of the vertical pore pressure gradient was observed across all cases of D_{50} = 0.33 mm sandbar owing to the different loose and medium-dense sediment compaction conditions. The vertical pore pressure gradients under loose (C7) compaction conditions were higher than those under medium-dense (C8) conditions.

Fig. 5.3 shows the variation of the maximum horizontal pore pressure gradient ($\partial p/\partial x_{\max}$) at different time steps and wave steepness values under

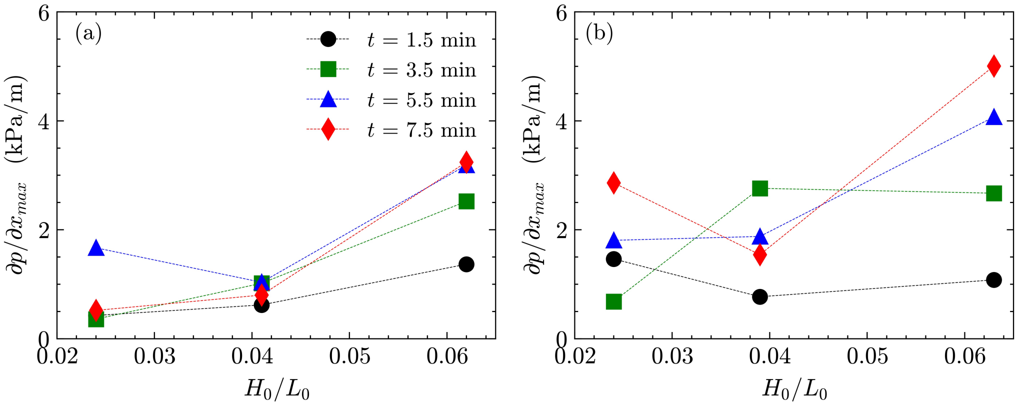

Figure 5.3: Maximum horizontal pore pressure gradient ($\partial p/\partial x_{\text{max}}$) as a function of wave steepness (H_0/L_0) at different time steps under (a) loose and (b) medium-dense compaction conditions.

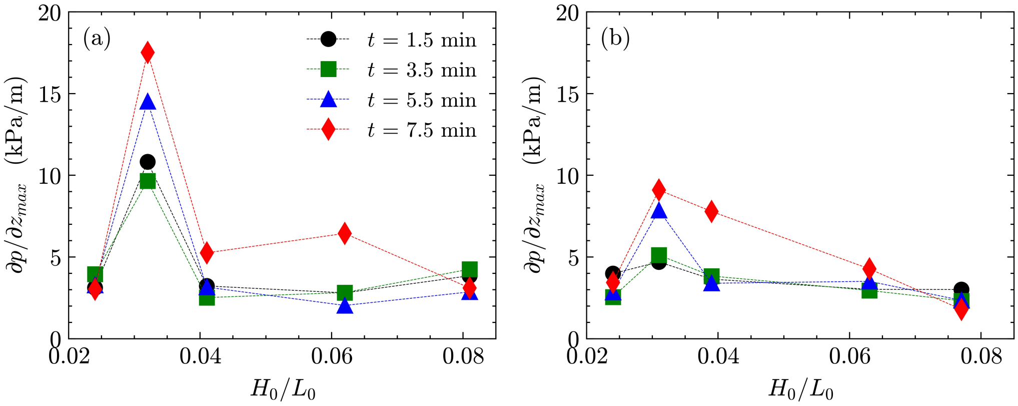

Figure 5.4: Maximum vertical pore pressure gradient ($\partial p/\partial z_{\text{max}}$) as a function of wave steepness (H_0/L_0) at different time steps under (a) loose and (b) medium-dense compaction conditions.

loose and medium-dense compaction conditions. At $t = 1.5$ min, the lowest $\partial p/\partial x_{\text{max}}$ was observed under loose compaction conditions (Fig. 5.3a), and there was no significant change in $\partial p/\partial x_{\text{max}}$ with increasing time for wave steepness (H_0/L_0) values of 0.024 and 0.041. However, at a wave steepness value of 0.063 there was a significant spread in $\partial p/\partial x_{\text{max}}$ values for different time steps. Overall, $\partial p/\partial x_{\text{max}}$ increased with the wave steepness.

Conversely, in medium-dense compaction conditions, the $\partial p/\partial x_{\text{max}}$ values were relatively higher compared to those under loose compaction conditions (Fig.5.3b). These $\partial p/\partial x_{\max}$ values were derived from the two pressure transducers (PT_1 and PT_2), which were positioned at the same depth ($z' = 1.5$ cm) from the top surface of the sandbar and were spaced 2 cm apart horizontally. The initial sandbar profile for medium-dense compaction exhibited rippling, resulting from 10 min of wave action in loose compaction conditions. This rippling was attributed to excessive wave-sediment interaction at $z' = 1.5$ cm during wave breaking, causing surface erosion and further rippling formation. For this reason, a negligible increase in shear strength (average 0.4 kN/m^2) was observed at $z' = 1.5$ cm under different H_0/L_0 conditions, as shown in previous chapter (see Fig. 4.7). The high sediment mobility at this depth likely contributed to super-porosity accumulation, leading to increased pore pressure and consequently higher $\partial p/\partial x_{\max}$ values. Specifically, in medium-dense compaction conditions, the average $\partial p/\partial x_{\max}$ values were 2.4, 2.7, and 1.4 times higher than loose compaction conditions at the wave steepness of 0.024, 0.041, and 0.062, respectively.

The variation of the maximum vertical pore pressure gradient ($\partial p/\partial z_{\max}$) at different time steps for different wave steepness values under loose and medium-dense compaction conditions is shown in Fig. 5.4. $\partial p/\partial z_{\max}$ values showed little change across the different wave steepness values at all time steps under both loose and medium-dense conditions except for a wave steepness of 0.032 (Figs. 5.4a and b), when there was a sudden increase in the pore pressure gradient, which increased with increasing time-steps. This deviation may be attributed to the combination of high wave height ($H = 10$ cm) and long wave periods ($T = 1.8$ s) in a 13.5 cm water column above the sandbar, which caused a significant increase in the erosion volume. However, this deviation was smaller under medium-dense compared to the loose compaction conditions. In loose compaction conditions, the average $\partial p/\partial z_{\max}$ values at $H_0/L_0 = 0.024, 0.032, 0.041, 0.062$, and 0.081 were 1.1, 2.0, 1.1, 1.0, and 1.4 times higher, respectively, than the medium-dense compaction conditions.

5.1.3 Amplitude Attenuation and Corresponding Phase Lag

Fig. 5.5 shows the variation of pore pressure amplitude attenuation ($|p|/p_0$) and corresponding phase lag ($\Delta\theta$) at $t = 3.5$ min for cases C5, C6, C7, C8, C9, and C10 under both compaction conditions. The symbol $|p|$ is the peak phase-averaged pore pressure occurring at different sediment depths (z'), and p_0 is the peak phase-averaged pore pressure at $z' = 1.5$ cm.

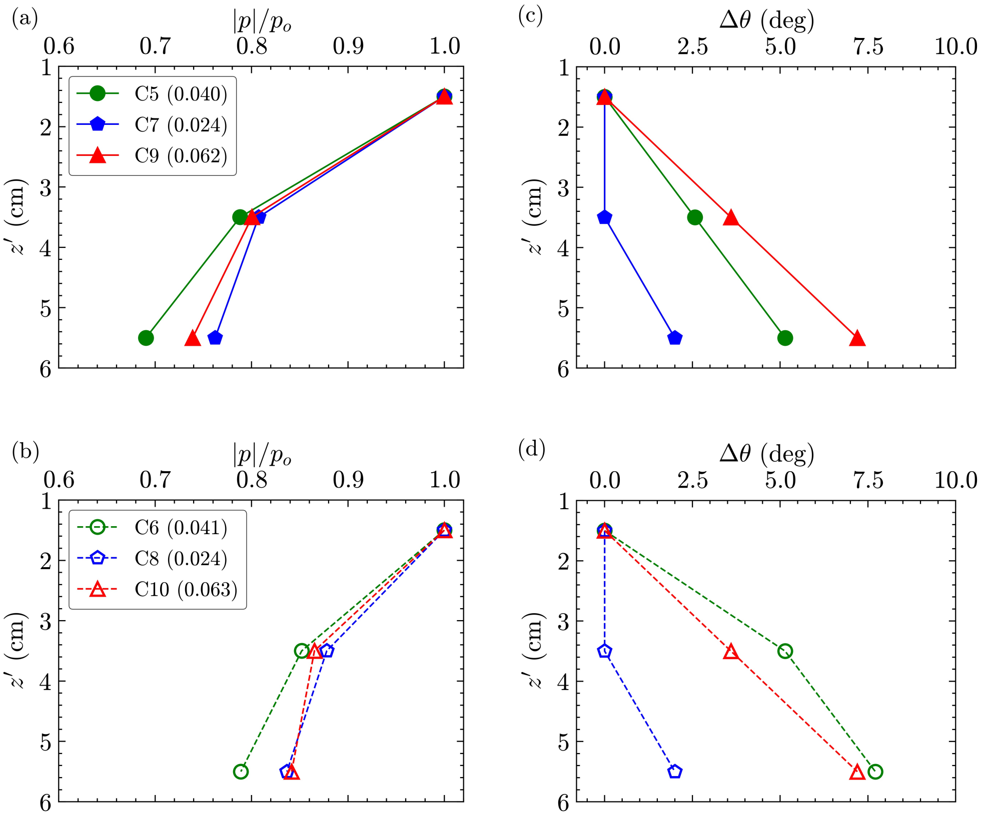

Figure 5.5: Amplitude attenuation of pore pressure ($|p|/p_0$) and phase lag ($\Delta\theta$) as a function of sediment depth for different wave steepness values: (a) and (c) under loose compaction conditions; (b) and (d) under medium-dense compaction conditions. Wave steepness values are shown in parentheses in the inset legends.

Fig. 5.5a shows that $|p|/p_0$ decreased as the sediment depth increased. Similar behavior was also reported by Li and Gao (2022). The amplitude attenuation shows little change under loose compaction conditions at $z' \leq 3.5$

cm, but more scattered values were observed at $z' \geq 3.5$ cm for the different wave steepness values. Under medium-dense compaction conditions, there was an increase in amplitude attenuation for the cases C6, C8, and C10, measuring 8.1 %, 8.8 %, and 8.1 % at $z' = 3.5$ cm and 14.3 %, 9.8 %, and 13.9 % at $z' = 5.5$ cm, respectively, as shown in Fig. 5.5b.

The phase lag ($\Delta\theta^\circ$) was calculated using $\Delta\theta = 360\,(\Delta T/T)$, where ΔT is the corresponding time difference between peak pore-pressures, and T denotes the wave periods. Under loose compaction (Fig. 5.5c), an increase in phase lag was observed with increasing sediment depth, particularly for cases C5 and C9. For case C7, no phase lag was observed at $z' \leq 3.5$ cm due to the very small wave steepness (0.024). Similar behavior was observed under medium-dense compaction conditions (Fig. 5.5d).

5.2 Quantification of Liquefaction Parameters

This section investigates the influence of wave stiffness on liquefaction index and liquefaction thickness under loose and medium-dense compaction conditions. It also analyses the quantity of erosion depth compared to the critical liquefaction thickness. The analysis of liquefaction parameters focuses on specific cases involving $D_{50} = 0.33$ mm sandbar only. These cases include loose compaction conditions (C1, C5, C7, and C9) and medium-dense compaction conditions (C2, C6, C8, and C10).

5.2.1 Liquefaction Index

The liquefaction index (Y) for loose and medium-dense compaction conditions was calculated using Eq. 2.2 at different pore pressure observation depths. Fig. 5.6 represents the liquefaction index with respect to different sediment depths. At $z' = 1.5$ cm, the magnitude of the liquefaction index was extremely high as this layer was mostly eroded during the experiment. The liquefaction index significantly decreased with increasing sediment depth because the excess pore pressure decreased with sediment depth as described in the section 5.1.1. At greater depths, the liquefaction index of medium-dense compaction showed nearly the same as that of loose compaction conditions. Although the liquefaction index varies with the sediment depth, there was a somewhat lower trend in the liquefaction index with higher wave steepness.

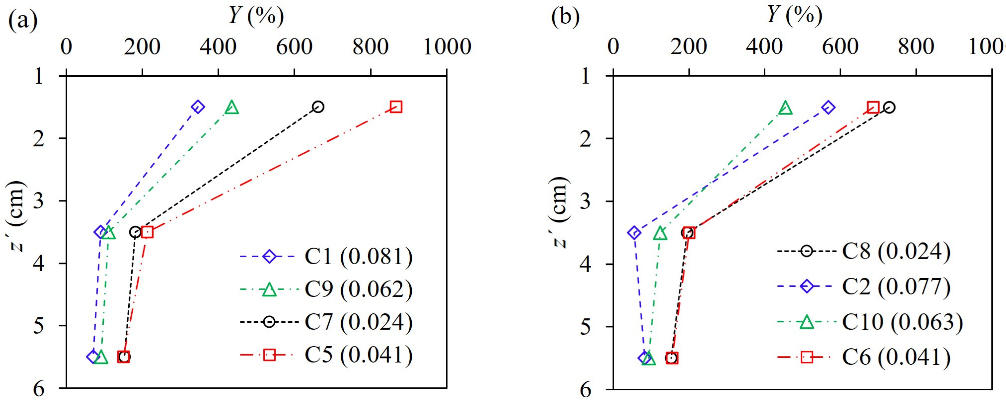

Figure 5.6: Variation of liquefaction index with respect to different sediment depth under (a) loose compaction and (b) medium-dense compaction.

5.2.2 Liquefaction Thickness

Critical liquefaction thickness (z) was calculated using Eq. 2.3 for both loose and medium-dense compaction conditions. In the saturated condition, the coefficient of earth pressure at rest (K_0) for loose and medium-dense compaction conditions was 0.46 and 0.36, respectively. The submerged unit weight (γ') was determined from the modeled ground (44.5 cm × 32 cm × 15 cm). The estimated value of γ' for loose and medium-dense compaction conditions was 8.87 kN/m^3 and 9.97 kN/m^3, respectively. Table 5.1 represents the critical liquefaction thickness of the sandbar in loose compaction conditions. From the calculated data, it was found that the decrease in wave height yielded the decrease in liquefaction thickness. In loose compaction conditions, the maximum and minimum critical liquefaction thicknesses were 7.8 cm (C1) and 3.4 cm (C7), respectively. A similar result was demonstrated by Yang et al. (2019), as the maximum liquefaction thickness of the soil was 4 cm considering $H = 7$ cm and $T = 1$ s. Additionally, considering the same wave height, the decreasing critical liquefaction thickness with increasing wave periods was observed throughout the experiment, which is identical to Chowdhury et al. (2006).

Table 5.1: Critical liquefaction thickness under loose compaction conditions

Cases	H (cm)	T (s)	L_0 (m)	z (cm)
C1	10	1.0	1.39	7.8
C5	10	1.4	2.28	5.4
C9	8	1.0	1.39	6.1
C7	8	1.8	3.15	3.4

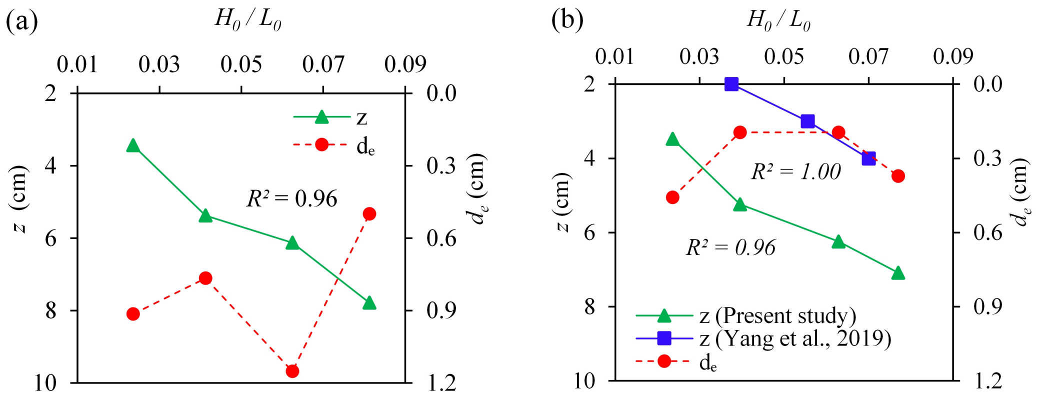

Figure 5.7: Variation of critical liquefaction thickness and sandbar erosion depth in different wave steepness under (a) loose compaction and (b) medium-dense compaction conditions.

Fig. 5.7 represents the correlation between the critical liquefaction thickness (z) and wave steepness (H_0/L_0). It was found that an increase in wave steepness yielded an increase in critical liquefaction thickness in both compaction conditions. A strong correlation ($R^2 = 0.96$) existed between them in both compaction conditions. In addition, the local erosion depth (d_e) of sandbar at the same cross-shore location (x = 200 cm) of pressure transducer are plotted in both compaction condition, as shown by red dashed line. In loose compaction conditions, an average of 16.5 % of the liquefied thickness was eroded during the wave action.

From the experimental data of Yang et al. (2019), the critical liquefaction thickness was plotted against their corresponding wave steepness, as shown in Fig. 5.7b. A similar increasing trend was found; however, the value of critical liquefaction thickness was smaller than the present study. The grain size of the soil was the possible reason for smaller value as Yang et al. (2019) used the composition of kaolin and fine silt (average diameter = 9.5 μm) and the present study was conducted by using the medium sand (D_{50} = 0.33 mm). The higher porosity of the silty soil resulted in lower liquefaction thickness due to the less pore pressure accumulation (Liu et al., 2019; Jia et al., 2014). In addition, considering the local erosion depth of sandbar, an average of 6.3 % of the liquefied thickness was eroded during the wave action under medium-dense compaction conditions.

5.3 Sediment Concentration

This section investigates the influence of sediment sizes (D_{50} = 0.33 mm and D_{50} = 0.08 mm) on sediment concentration. It delves into the correlation between average sediment concentration and wave steepness. Furthermore, it examines the relationship between phase-averaged sediment concentration and water surface elevation.

5.3.1 Sediment Concentration Time Series

Fig. 5.8 illustrates the time series of sediment concentration (C) for sandbars with D_{50} = 0.33 mm and 0.08 mm under loose compaction conditions. For the D_{50} = 0.33 mm sandbar, sediment concentration exhibited distinct fluctuations despite different wave conditions in cases C1, C5, and C7, characterized by wave steepness (H_0/L_0) values of 0.081, 0.041, and 0.024, respectively. The average sediment concentrations were 2.5 g/L for C1, 9.2 g/L for C5, and 7.8 g/L for C7. In contrast, the D_{50} = 0.08 mm sandbar consistently remained in suspension due to its lower settling velocity compared to the D_{50} = 0.33 mm sandbar. Consequently, significantly higher sediment concentration was observed in this case, with 10 min average concentration of 27.3 g/L for C1a, 51.9 g/L for C5a, and 16.5 g/L for C7a.

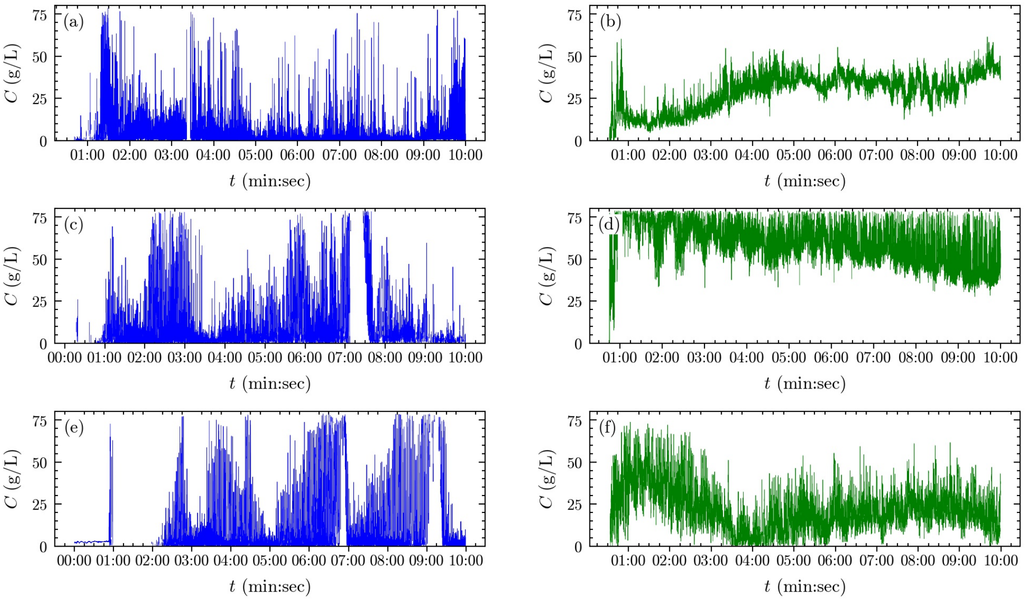

Figure 5.8: Time series of sediment concentration in different sediment sizes. Sub-figures a, c, and e show cases C1, C5, and C7, respectively, for a D_{50} of 0.33 mm sandbar. Sub-figures b, d, and f depict cases C1a, C5a, and C7a, respectively, for a D_{50} of 0.08 mm sandbar.

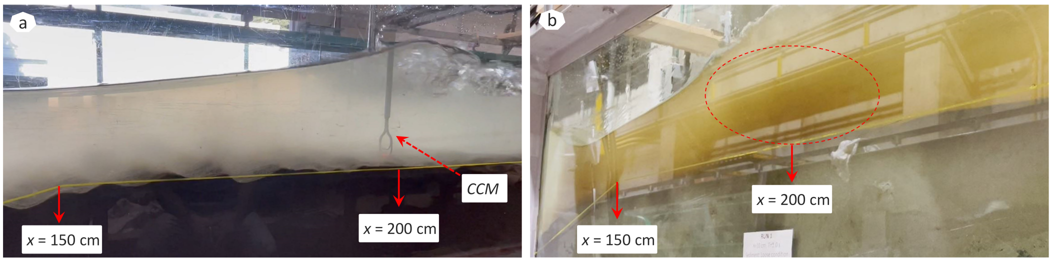

Figure 5.9: Real-time illustrations of sediment concentration during wave propagation for (a) D_{50} = 0.33 mm: case C1 and (b) D_{50} = 0.08 mm: case C1a. *CCM* stands for conductivity concentration meter.

For better understanding of the effect of sediment size, Fig. 5.9 represents the real-time observations of sediment concentration. During the wave action, very little suspended sediment was observed in the water column with D_{50} = 0.33 mm, as shown in Fig. 5.9a. In contrast, Fig. 5.9b shows that very fine sediment particles of D_{50} = 0.08 mm exhibited significant movement of suspended particles around the conductivity concentration meter

(CCM) due to breaking waves, leading to higher concentrations, as indicated by the red dashed circle. Sato et al. (1990) note that at the breaking point, turbulence and large-scale vortices create a high-concentration sand cloud. This comparison emphasize the elevated concentrations and enhanced suspension tendency associated with finer sediment particles at the breaking point.

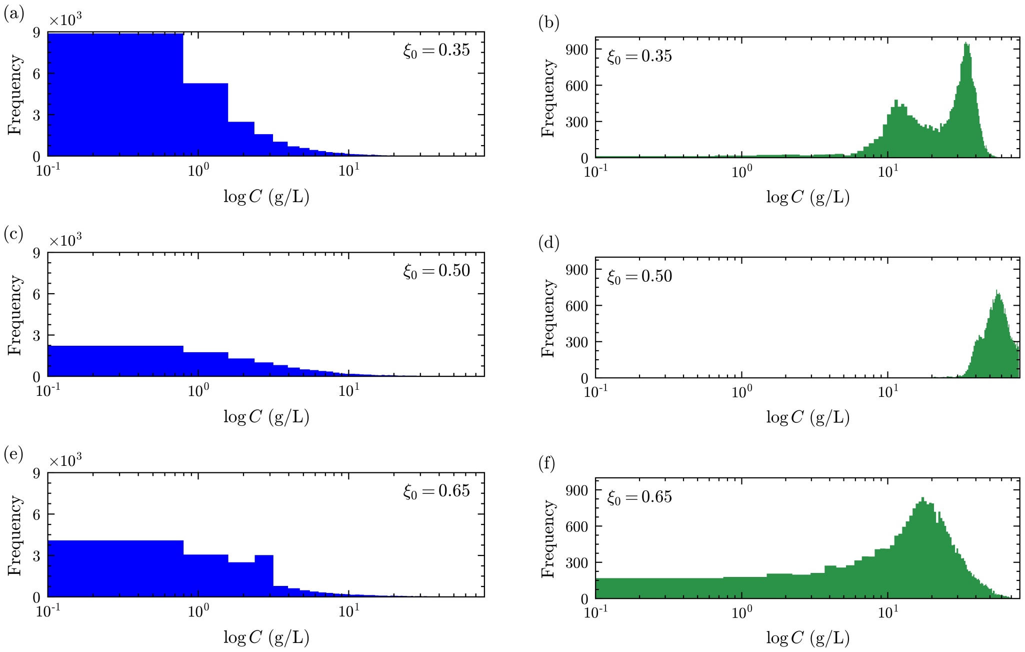

Figure 5.10: Histograms of sediment concentration (C) under different sediment sizes. Sub-figures a, c, and e show cases C1, C5, and C7, respectively, for a D_{50} of 0.33 mm sandbar. Sub-figures b, d, and f depict cases C1a, C5a, and C7a, respectively, for a D_{50} of 0.08 mm sandbar. The x-axis is shown as a logarithmic scale.

5.3.2 Sediment Concentration Histogram

Fig. 5.10 shows the histogram or frequency distribution of concentration (C) under loose compaction for sediment sizes D_{50} = 0.33 mm and 0.08 mm. For the D_{50} = 0.33 mm sandbar, the sediment concentration patterns were consistent across various wave conditions (Fig. 5.10 a, c, and e), although maximum frequencies varied with the type of wave breaking. In case C1 (spilling wave breaking, $\xi_0 = 0.35$), sediment concentration exhibited a uniform distribution peaking at 8800 Hz between 0 and 0.8 g/L (Fig. 5.10a). In cases C5 and C7 (plunging wave breaking), a similar uniform distribution was observed at the peak frequencies of 2250 and 4000, respectively.

In contrast, the histogram for $D_{50} = 0.08$ mm sandbar showed a different trend despite similar wave conditions (Fig. 5.10 b, d, and f). In case C1a, sediment concentrations ranged widely from 6 to 55 g/L, with a peak around 38 g/L, and a notably lower maximum frequency of 900 compared to the $D_{50} = 0.33$ mm sandbar (Fig. 5.10b). For plunging waves in case C5a, concentrations ranged from 30 to 78 g/L, peaking at 55 g/L with a maximum frequency of 700 (Fig. 5.10d). Case C7a exhibited a wide dispersion of sediment concentration from 0 to 50 g/L, with the highest concentration at 19 g/L (Fig. 5.10f) .

5.3.3 Average Sediment Concentration

To compare the impact of wave steepness, the average sediment concentration (C_{avg}) was calculated over the 10 min duration of wave action. Fig. 5.11 shows the variation in average sediment concentration with wave steepness (H_0/L_0) under loose and medium-dense compaction conditions. Under loose compaction of D_{50}= 0.33 mm sandbar, the maximum average concentration was 13.2 g/L with a wave steepness of 0.031. The average sediment concentration was lower under medium-dense compaction conditions for the same sediment size.

In comparison to $D_{50} = 0.33$ mm sandbar, $D_{50} = 0.08$ mm sandbar resulted in extremely higher average sediment concentration under loose compaction conditions. In addition, a wide range of variation was observed in average sediment concentration between loose and medium-dense compaction conditions. The medium-dense compaction conditions resulted in comparatively higher average sediment concentration than loose compaction at H_0/L_0 of 0.024 and 0.081. For comparison with the present study, the experimental results of Tabasi et al. (2021) for very fine sand ($D_{50} = 0.08$ mm) are plotted in the same figure. In case of $D_{50} = 0.08$ mm, the lower values observed in Tabasi et al. (2021)'s experiment can be attributed to the effect

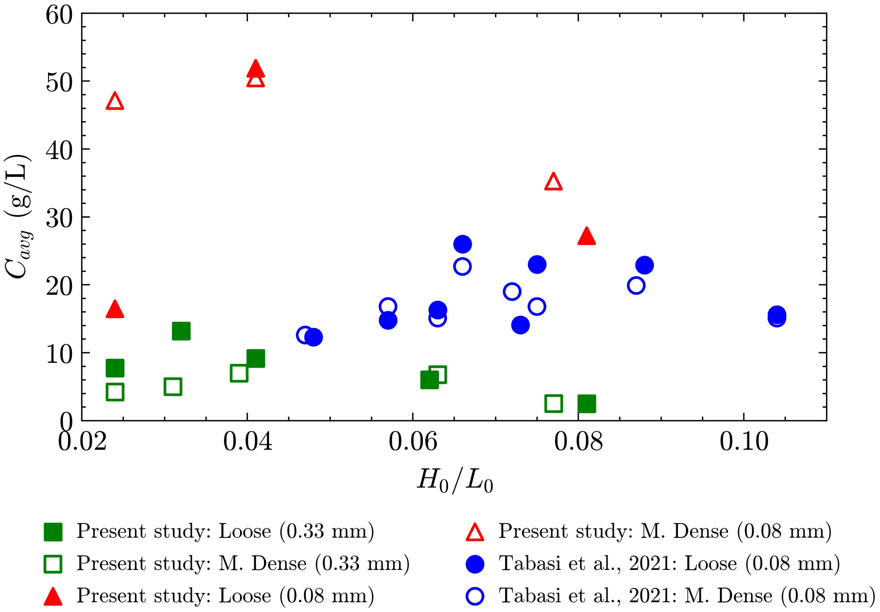

Figure 5.11: Average sediment concentration (C_{avg}) as a function of wave steepness (H_0/L_0). The results from this study are shown as rectangular markers for D_{50} = 0.33 mm and triangular markers for D_{50} = 0.08 mm. The findings from Tabasi et al. (2021) are represented as circular markers.

of the non-breaking conditions. The present study involved spilling and plunging type of breaking conditions, unlike the experiment conducted by Tabasi et al. (2021), which was carried out under non-breaking conditions. Moreover, it was difficult to find a linear correlation between the average sediment concentration and wave steepness.

5.3.4 Phase-Averaged Sediment Concentration

To understand the temporal variation in the sediment concentration, the phase-averaged concentration was computed at time steps t = 1.5, 3.5, 5.5, and 7.5 min. A time step t = 3.5 min was selected to ensure consistency, particularly because the discussion of the phase-averaged pore pressure gradient also takes place at this same time step in the subsection 5.1.1. Fig. 5.12 shows the phase-averaged concentration (C_t) at t = 3.5 min under loose (case C7) and medium-dense (case C8) compaction conditions for D_{50} = 0.33 mm. The sediment concentration and water surface elevation (η) are presented at the same time for the 10 wave periods in Figs. 5.12a and d.

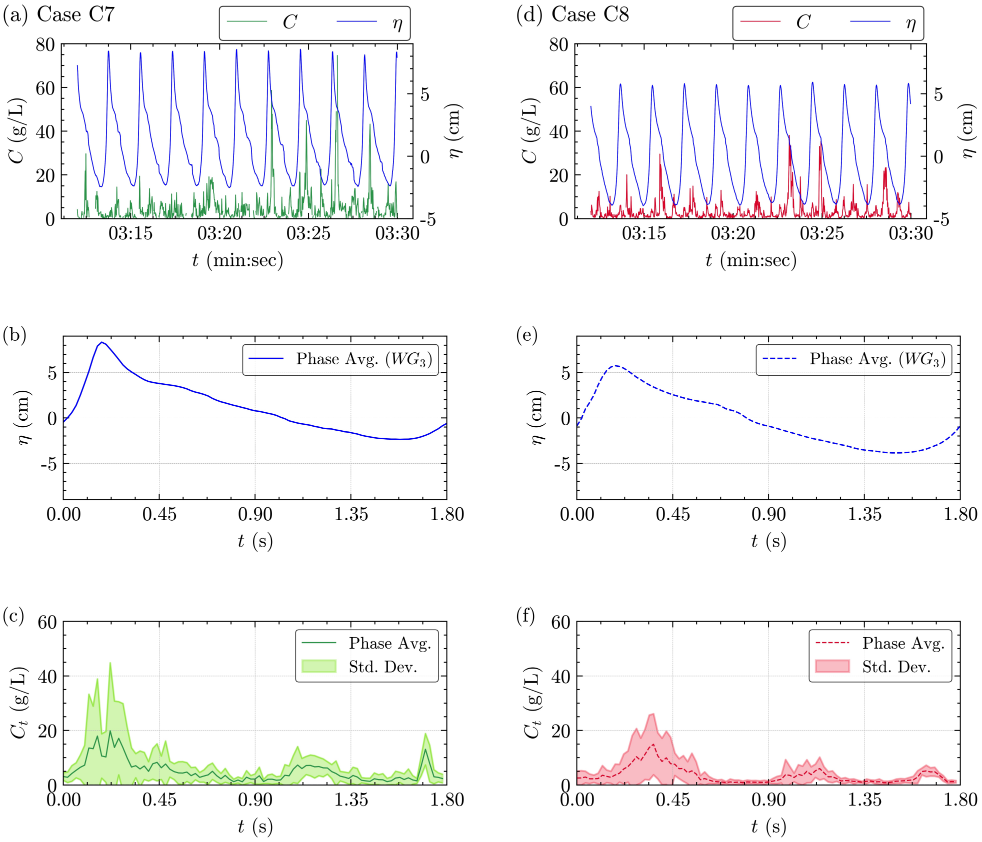

Figure 5.12: Phase-averaged concentrations for D_{50} = 0.33 mm sandbar under loose and medium-dense compaction conditions. Subfigures (a), (b), and (c) are for case C7 with loose compaction, while (d), (e), and (f) are for case C8 with medium-dense compaction.

In Fig. 5.12a, for case C7, there was a rising trend of concentration after t = 3 min 23 s and maximum value occurred at t = 3 min 26 s. Loose compaction condition of sandbar (Initial τ_{mid} = 4.57 kN/m^2) with plunging type wave breaking (impinging zone, x = 245 to 275 cm) are the possible reasons for the sudden increase in concentration value. Conversely, in Fig. 5.12b, the peak concentration value of case C8 was significantly lower than case C7 due to the medium-dense compaction conditions (Initial τ_{mid} = 7.76 kN/m^2). In phase-average analysis of sediment concentration (Figs. 5.12c and f), the highest phase-averaged concentration was observed beneath the wave crest, while the lowest concentration was observed beneath the wave trough, primarily due to the suspended sediment aligning with wave shapes during their back-and-forth movement. Wave crests, with high-water columns, exhibited elevated sediment concentration. This phenomenon might be influenced by the type of wave breaking (Table 3.3). Although a similar pattern was observed under both loose and medium-dense compaction conditions, a somewhat higher phase-averaged concentration beneath the wave crest was observed under loose compaction than under medium-dense compaction condition. A high standard deviation at the peak indicates greater variability in the data points around the peak concentration beneath the wave crest.

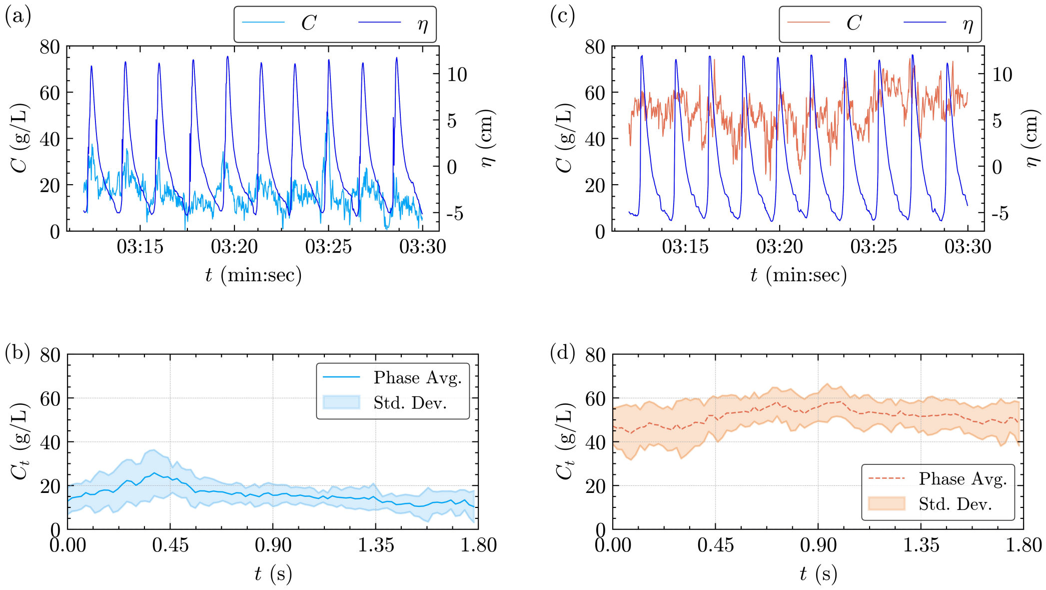

Figure 5.13: Phase-averaged concentrations for $D_{50} = 0.08$ mm sandbar under loose and medium-dense compaction conditions. Subfigures (a) and (b) are for case C7a with loose compaction, while (c) and (d) are for case C8a with medium-dense compaction.

Fig. 5.13 shows the phase-averaged concentration at $t = 3.5$ min for the $D_{50} = 0.08$ mm sandbar under loose (case C7a) and medium-dense compaction (case C8a) conditions. A clear effect of wave crest and wave trough was absent on the concentration in both compaction conditions. A nearly uniform phase-averaged sediment concentration was observed in both loose compaction and medium-dense compaction conditions. Compared to the loose compaction (Fig. 5.13b), a significantly higher phase-averaged concentration value was observed in the medium-dense compaction(Fig. 5.13d). The possible reason for this kind of higher trend is the very fine particle density within the compaction condition of the ground. In the case of loose compaction, a higher dispersion of fine particles was observed in water during wave actions. As a result, the movement of eroded sediment particles during wave actions was impeded by the presence of very fine dispersed particles, leading to a decreased concentration near the concentration meter, as shown in Fig. 5.9b. Conversely, in medium-dense compaction conditions, these dispersed particles settled and contributed to the formation of a more densely compacted ground. During the wave action, the eroded sediment moved near the concentration meter, exhibiting a higher concentration.

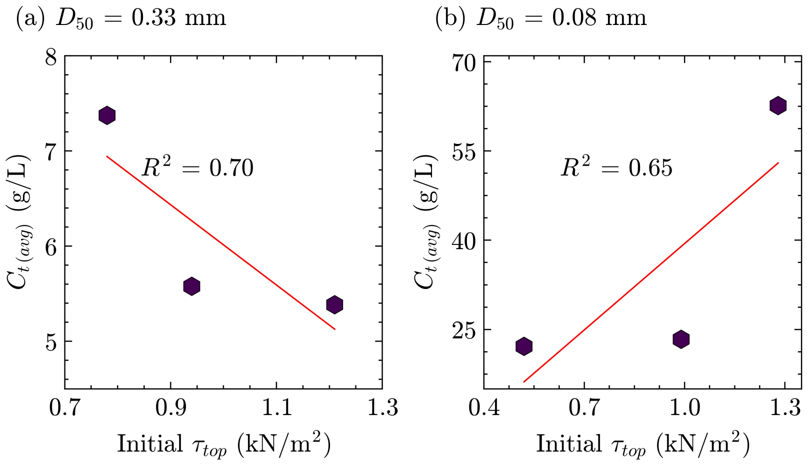

Figure 5.14: Mean phase-averaged sediment concentration as a function of the initial shear strength of the top layer of the sandbar.

For understanding the effect of initial shear strength on phase-averaged concentration, the mean phase-averaged concentration ($C_{t(avg)}$) is plotted with the initial shear strength (Initial τ_{top}) under loose compaction conditions (Fig. 5.14). In the case of the sandbar with $D_{50} = 0.33$ mm, a good inverse correlation ($R^2 = 0.70$) was observed. This phenomenon aligns with the natural trend: when the ground is highly compacted, the sediment concentration tends to be lower. This inverse relationship occurs because more compacted sediments are less easily mobilized by wave action, resulting in a lower sediment concentration.

Conversely, the sandbar with D_{50} = 0.08 mm exhibited substantial erosion due to wave breaking as mentioned in chapter 4 (see section 4.1). This erosion was accompanied by a consistently higher sediment concentration, which may help explain the observed correlation ($R^2 = 0.65$). The finer sand particles (D_{50} = 0.08 mm) are more easily mobilized by wave action, leading to greater sediment transport and erosion, thereby influencing the relationship between the observed parameters. Compared to the sandbar with $D_{50} = 0.33$, the significant effect of wave breaking on sediment concentration in the $D_{50} = 0.08$ sandbar may account for the observed trend, regardless of the initial shear strength.

5.4 Inter-dependency of Fundamental Parameters

5.4.1 Average Erosion Volume and Concentration

Fig. 5.15 illustrates the correlation between the erosion volume of the sandbar (ΔV_e) and average sediment concentration (C_{avg}) under loose and medium-dense compaction conditions. The color bar represents the varying initial shear strength (τ_{top}) at the top layer of the sandbar ($z' = 1.5$ cm). In instances where a higher initial shear strength was present under loose compaction conditions, both a lower erosion volume and lower average sediment concentration were observed for the sandbar. However, a deviation in these patterns became evident during the reduction of the initial shear strength. Regardless of the initial shear strength, a strong correlation ($R^2 = 0.84$ for $D_{50} = 0.33$ mm and $R^2 = 1$ for $D_{50} = 0.08$ mm) was established between the erosion volume and average sediment concentration (Figs. 5.15a and b).

In the case of medium-dense compaction of D_{50} = 0.33 mm sandbar, the observed values were more scattered, and no correlation was observed (Fig. 5.16a). In this case, the initial shear strength at the top layer of sandbar (τ_{top}) was, on average, 1.5 times higher than the loose compaction conditions. This substantial difference in initial shear strength contributed to a notable reduction in erosion volume under medium-dense compaction con-

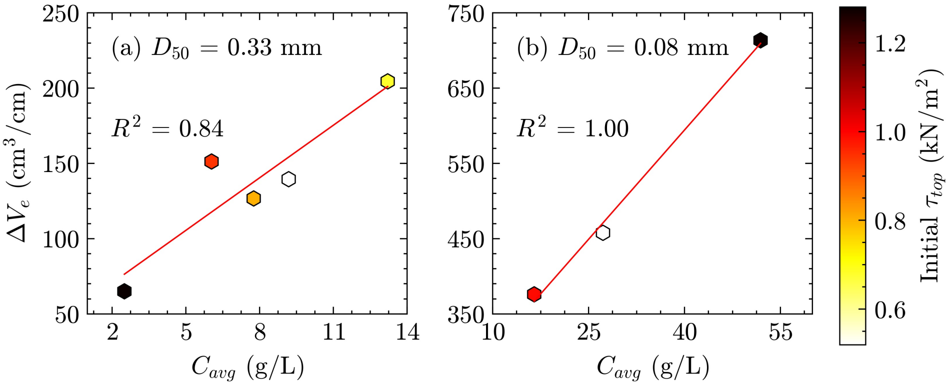

Figure 5.15: Correlation between erosion volume (ΔV_e) and average sediment concentration (C_{avg}) for (a) D_{50} = 0.33 mm and (b) D_{50} = 0.08 mm under loose compaction conditions. The color bar shows the initial shear strength (τ_{top}) at the top layer (z' = 1.5 cm) of the sandbar.

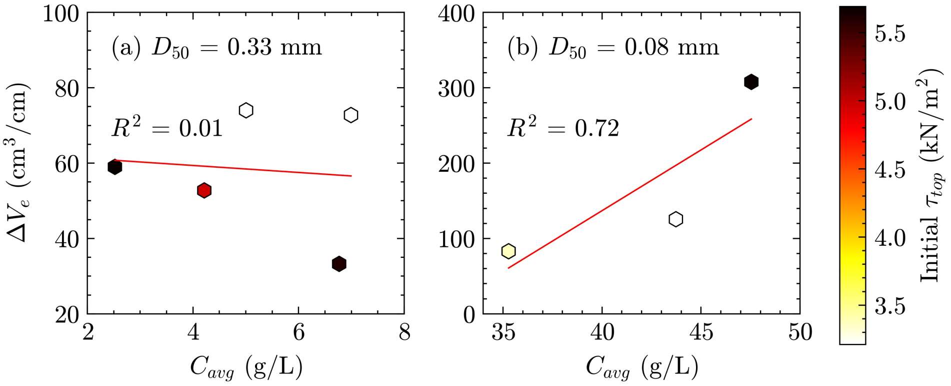

Figure 5.16: Correlation between erosion volume (ΔV_e) and average sediment concentration (C_{avg}) for (a) D_{50} = 0.33 mm and (b) D_{50} = 0.08 mm under medium-dense compaction conditions. The color bar shows the initial shear strength (τ_{top}) at the top layer (z' = 1.5 cm) of the sandbar.

ditions, as presented in Fig. 4.5. Furthermore, as highlighted in a previous chapter (Table 4.1), there was a lack of correlation (R^2 = 0.001) between change in shear strength and wave steepness for the same sandbar setup with D_{50} = 0.33 mm when subjected to medium-dense compaction conditions. These factors are considered potential reasons contributing to the absence of a correlation under medium-dense compaction conditions of D_{50} = 0.33 mm sandbar. In contrast, a strong correlation (R^2 = 0.72) was established in the case of a sandbar with sediment size of D_{50} = 0.08 mm (Fig. 5.16b). The substantial sandbar erosion volume induced by wave breaking, coupled with a consistently higher sediment concentration (Fig. 5.13d), could be a possible reason for the observed strong correlation in this case.

5.4.2 Phage-averaged Pressure Gradient and Concentration

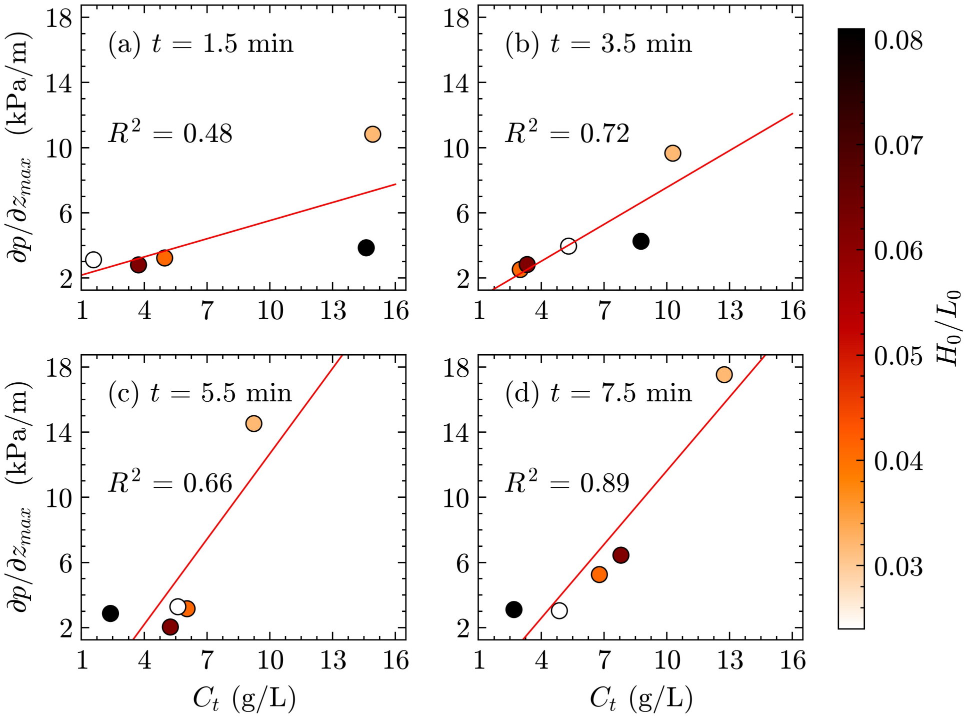

Figure 5.17: Correlation between maximum vertical pore pressure gradient ($\partial p/\partial z_{\max}$) and phase-averaged sediment concentration (C_t) under loose compaction conditions at different time steps: (a) t = 1.5 min, (b) t = 3.5 min, (c) t = 5.5 min, and (d) t = 7.5 min. The color bar shows the different wave steepness values.

Fig. 5.17 shows the dynamic correlation between the maximum vertical pore pressure gradient ($\partial p/\partial z_{\max}$) and phase-averaged sediment concentration (C_t) at different time steps under loose compaction conditions. The color bar represents the different wave steepness values. Four time-steps were selected to determine the dynamic correlation at t = 1.5, 3.5, 5.5, and

7.5 min. At the beginning of the wave actions (t = 1.5 min), rippling began to occur, and the sediment concentration was higher owing to the loose compaction condition in the top layer of the sandbar, which explains the slightly lower correlation coefficient (R^2 = 0.48), as shown in Fig. 5.17a. As the duration of the wave action increased, sandbar erosion resulted from breaking waves, and concurrently, the sediment concentration increased as the maximum vertical pore pressure gradient increased (Fig. 5.4a). Regardless of the wave steepness, the strongest correlation (R^2 = 0.89) was established between the maximum vertical pore pressure gradient and the phase-averaged sediment concentration at t = 7.5 min (Fig. 5.17d).

Conversely, a notably weak correlation was identified between the maximum vertical pore pressure gradient and the phase-averaged sediment concentration under medium-dense compaction conditions. The correlation coefficients R^2 were 0.0005, 0.2034, 0.0002, and 0.0287 at t = 1.5, 3.5, 5.5, 7.5 min, respectively. From Fig. 5.4b, it was evident that the maximum pore pressure gradient increased with the duration of the wave actions. Nevertheless, owing to the changing shapes of the initial sandbar profiles under medium-dense compaction conditions, the phase-averaged sediment concentration exhibited both increasing and decreasing variability over time. This may have contributed to the low correlation coefficient in the dynamic correlation analysis.

5.5 Summary of the Findings

1. The magnitude of excess pore pressure was greater in longer wave periods than that of shorter periods considering the same wave height. A decreasing trend of liquefaction index was observed with increasing sediment depth. The liquefaction index exhibited nearly identical values under both compaction conditions at greater sediment depth.

2. An increase in wave steepness resulted in an increase in the critical liquefaction thickness under both compaction conditions. A strong correlation (R^2 = 0.96) was established between the critical liquefaction thickness and wave steepness under both compaction conditions.

In loose compaction conditions, an average of 16.5 % of the liquefied thickness was eroded. On the other hand, an average of 6.3 % of the liquefied thickness was eroded in medium-dense compaction conditions.

3. There was little change in the phase-averaged pore pressures observed in the horizontal *PT* array. Conversely, a significant decrease was observed in the phase-averaged pore pressure in the vertical *PT* array as the sediment depth increased.

4. In contrast to the loose compaction, the medium-dense compaction conditions exhibited relatively higher maximum horizontal pressure gradient. However, in the case of maximum vertical pressure gradient, loose compaction conditions showed relatively higher values.

5. As sediment depth increased, a decreasing non-linear trend in amplitude attenuation and a corresponding increase in phase-lag were observed, indicating that shallow depths are more dynamic and prone to rapid changes compared to deeper layers.

6. A significantly higher phase-averaged sediment concentration was observed beneath the wave crest. A poor correlation was established between the sandbar erosion volume and the surf similarity parameter under loose and medium-dense compaction conditions. However, a strong correlation ($R^2 = 0.84$) was established between the sandbar erosion volume and average sediment concentration under loose compaction conditions.

7. In a dynamic correlation analysis, a strong correlation ($R^2 = 0.89$) was established between the maximum vertical pressure gradient and phase-averaged sediment concentration at $t = 7.5$ min under loose compaction conditions.

Chapter 6

Conclusions

6.1 Concluding Remarks

In recent years, the addition of filling sand over sandbars in the form of submerged artificial sandbars has been explored as a nature-based solution for reducing shore erosion. This dissertation aimed to explore sandbar dynamics by considering pore pressure gradients, sediment concentration, and bed-level erosion through an innovative experimental method. Three specific objectives were addressed, each contributing to a deeper understanding of sandbar dynamics.

The first specific objective investigated the impact of sediment size on sandbar morphology, focusing on erosion susceptibility and shear strength. The results demonstrated that sandbar with very fine sand (D_{50} = 0.08 mm) were more prone to erosion than those with medium sand (D_{50} = 0.33 mm) due to wave breaking mechanisms. Sandbars with medium sand exhibited erosion primarily at the off-shore sharp end, while those with very fine sand experienced erosion at the impinging point. Additionally, as wave steepness increased, sandbars with medium sand showed a strong inverse correlation between net erosion volume and wave steepness, while those with very fine sand exhibited a sharp peak. Moreover, the shear strength of the middle layer of sandbars with very fine sand was five times higher compared to those with medium sand. These findings emphasize the superior effectiveness of medium sand as filler materials of submerged artificial sandbars in enhancing the stability against wave action. Additionally, the datasets obtained are valuable for conducting numerical simulations.

The second specific objective delved deeper into sandbar dynamics by analyzing liquefaction parameters based on pore water pressure responses. Results revealed that the liquefaction index decreased as sediment depth increased. A strong correlation ($R^2 = 0.96$) was found between critical liquefaction thickness and wave steepness. During the 10 min of wave action, an average of 16.5 % of the liquefied thickness was eroded in loose compaction, whereas 6.3 % of the liquefied thickness was eroded in medium-dense compaction. These results underscore the importance of sediment compaction in influencing liquefaction potentiality and emphasize the need for a comprehensive field study of wave-induced liquefaction.

The third specific objective explored the effect of sediment compaction on wave-induced pore pressure gradients and sediment concentration. In order to comprehend the temporal change of these parameters, the discussions proceeded by examining the dynamic correlation between the phase-averaged pressure gradients and the sediment concentration. In case of medium sand, the results showed that there was a distinct pore pressure amplitude attenuation with a simultaneous rise in the phase lag, as sediment depth increased. Loosely compacted sandbars exhibited a 1.3 times higher maximum vertical pressure gradient than medium-dense formations. Sandbar with loose compaction conditions, a strong correlation was observed between erosion volume and average sediment concentration, alongside a dynamic correlation between the maximum phase-averaged vertical pressure gradient and sediment concentration. In terms of applications, understanding the impact of sediment compaction on wave-induced pressure gradients and sediment concentration empowers practitioners to make more informed decisions during beach nourishment project design and execution. Ultimately, integrating these insights into beach nourishment strategies can lead to more efficient and sustainable coastal management practices.

6.2 Limitations and Recommendations

The results from this controlled wave flume experiment demonstrate the potential applications of the artificial sandbar approach. However, when applying these findings to real-world coasts, it is crucial to consider external dynamic conditions and scale effects on local sediment transport. Notably, this laboratory study focused on specific aspects considering regular wave conditions, and while tidal effects, alongshore currents, and the effect of sediment turbulence were neglected.

To achieve a more precise representation of sandbar morphology, using a sandbar shape scaled down directly from field measurements would be beneficial. Future research could investigate erodible beach profiles alongside the actual sandbar shape for additional insights. The sediment size is another dominating factor in sandbar morphology as very fine sand is more erosive that medium sand. Mixing sediment sizes could be a potential consideration for future studies. Due to the vertical direction limitations of the wave flume in the laboratory, the mean water level remained same for all cases; however, variations in water depth above the sandbar crest should be taken into account.

In field studies of surf zone sandbars, investigating the influence of wave breaking on pore pressure accumulation, and subsequently, liquefaction potential could be a promising direction for future research. Installing additional concentration meters in the water column would help determine the maximum sediment suspension. Using a mobile cart to assess sediment concentration variations along cross-shore locations is also recommended. To accurately assess the contributions of dynamic compaction and overburden pressure at different depths within a sandbar, it is recommended to perform a detailed analysis that isolates these variables and examines their individual impacts on shear strength.

Moreover, this study provides valuable datasets that can be used to enhance and calibrate numerical models. For calibrating sandbar morphology, sediment concentration, and water surface elevation, XBeach and Delft3D models can be utilized. CADMUS-SURF 2D emerges as a promising choice for calibrating pressure responses based on laboratory datasets.

Bibliography

Anderson, D., Bak, A. S., Cohn, N., Brodie, K. L., Johnson, B., and Dickhudt, P. (2023). The Impact of Inherited Morphology on Sandbar Migration During Mild Wave Seasons. *Geophysical Research Letters*, 50(3).

Anderson, D., Cox, D., Mieras, R., Puleo, J. A., and Hsu, T. (2017). Observations of wave-induced pore pressure gradients and bed level response on a surf zone sandbar. *Journal of Geophysical Research: Oceans*, 122(6):5169–5193.

Battjes, J. (1974). Surf Similarity. In *Coastal Engineering 1974*, volume 1, pages 466–480, New York, NY. American Society of Civil Engineers.

Bryan, K. R., Davies-Campbell, J., Hume, T. M., and Gallop, S. L. (2019). The Influence of Sand Bar Morphology on Surfing Amenity at New Zealand Beach Breaks. *Journal of Coastal Research*, 87(sp1):44.

Chowdhury, B., Dasari, G. R., and Nogami, T. (2006). Laboratory Study of Liquefaction due to Wave–Seabed Interaction. *Journal of Geotechnical and Geoenvironmental Engineering*, 132(7):842–851.

Das, B. M. and Sobhan, K. (2014). *Principles of Geotechnical Engineering*. Cengage Learning, Massachusetts, 8 edition.

Demirci, M., Aköz, M. S., and Üneş, F. (2014). Experimental investigation of cross-shore sandbar volumes. *Journal of Coastal Conservation*, 18(1):11–16.

Du, X., Sun, Y., Song, Y., and Xiu, Z. (2020). Wave-induced liquefaction hazard assessment and liquefaction depth distribution: A case study in the Yellow River Estuary, China. *IOP Conference Series: Earth and Environmental Science*, 569(1).

Grasso, F., Michallet, H., and Barthélemy, E. (2011). Experimental simulation of shoreface nourishments under storm events: A morphological, hydrodynamic, and sediment grain size analysis. *Coastal Engineering*, 58(2):184–193.

Grossmann, F., Hurther, D., van der Zanden, J., Sánchez-Arcilla, A., and Alsina, J. M. (2023). Near-Bed Sediment Transport Processes During Onshore Bar Migration in Large-Scale Experiments: Comparison With Offshore Bar Migration. *Journal of Geophysical Research: Oceans*, 128(3):e2022JC018998.

Grunnet, N. M. and Ruessink, B. G. (2005). Morphodynamic response of nearshore bars to a shoreface nourishment. *Coastal Engineering*, 52(2):119–137.

Hamm, L., Capobianco, M., Dette, H., Lechuga, A., Spanhoff, R., and Stive, M. (2002). A summary of European experience with shore nourishment. *Coastal Engineering*, 47(2):237–264.

Islam, M. S. and Suzuki, T. (2023). Effect of sediment size on sandbar morphology in different compaction conditions. *Journal of JSCE*, 11(2):23–18100.

Islam, M. S. and Suzuki, T. (2024). Quantification of wave-induced liquefaction in small-scale surf zone sandbar. In Tajima, Y., Aoki, S.-i., and Sato, S., editors, *Proceedings of the 11th International Conference on Asian and Pacific Coasts*, pages 89–97, Singapore. Springer Nature Singapore.

Islam, M. S., Suzuki, T., and Thilakarathne, S. (2024). Physical modeling of sandbar dynamics to correlate wave-induced pore pressure gradient, sediment concentration, and bed-level erosion. *Ocean Engineering*, 307:118161.

Japanese Geotechnical Society (2015). *Laboratory Testing Standards of Geomaterial Vol. 1 (JGS 0161-2009)*. Maruzen publishing, Tokyo.

Jeng, D. (2001). Mechanism of the wave-induced seabed instability in the vicinity of a breakwater: a review. *Ocean Engineering*, 28(5):537–570.

Jia, Y., Zhang, L., Zheng, J., Liu, X., Jeng, D. S., and Shan, H. (2014). Effects of wave-induced seabed liquefaction on sediment re-suspension in the Yellow River Delta. *Ocean Engineering*, 89:146–156.

Kirca, V. S. O. and Ulker, M. B. C. (2014). Recent Developments on Wave-Induced Liquefaction of Marine Seabed. In *11th Int. Congress on Advances in Civil Eng.*, Istanbul, Turkey.

Kuang, C., Han, X., Zhang, J., Zou, Q., and Dong, B. (2021). Morphodynamic Evolution of a Nourished Beach with Artificial Sandbars: Field Observations and Numerical Modeling. *Journal of Marine Science and Engineering 2021, Vol. 9, Page 245*, 9(3):245.

Li, C. F. and Gao, F. P. (2022). Characterization of spatio-temporal distributions of wave-induced pore pressure in a non-cohesive seabed: Amplitude-attenuation and phase-lag. *Ocean Engineering*, 253:111315.

Li, Y., Zhang, C., Dai, W., Chen, D., Sui, T., Xie, M., and Chen, S. (2022). Laboratory investigation on morphology response of submerged artificial sandbar and its impact on beach evolution under storm wave condition. *Marine Geology*, 443:106668.

Liu, T., Lu, Y., Zhou, L., Yang, X., and Guo, L. (2019). Experiment and analysis of submarine landslide model caused by elevated pore pressure. *Journal of Marine Science and Engineering*, 7(5).

Madsen, O. S. (1974). Stability of a Sand Bed under Breaking Waves. In *Coastal Engineering Proceedings*, volume 1, page 45. ASCE.

Madsen, O. S. and Durham, W. M. (2007). Pressure-Induced Subsurface Sediment Transport in the Surf Zone. In *Coastal Sediments '07*, pages 82–95, Reston, VA. American Society of Civil Engineers.

McDougal, W. G., Tsai, Y. T., Liu, P. L., and Clukey, E. C. (1989). Wave-induced pore water pressure accumulation in marine soils. *Journal of Offshore Mechanics and Arctic Engineering*, 111(1):1–11.

Mieras, R. S., Puleo, J. A., Anderson, D., Cox, D. T., and Hsu, T. (2017). Large-scale experimental observations of sheet flow on a sandbar under skewed-asymmetric waves. *Journal of Geophysical Research: Oceans*, 122(6):5022–5045.

Pan, Y., Kuang, C., Zhang, J., Chen, Y., Mao, X., Ma, Y., Zhang, Y., Yang, Y., and Qiu, R. (2017). Postnourishment Evolution of Beach Profiles in a Low-Energy Sandy Beach with a Submerged Berm. *Journal of Waterway, Port, Coastal, and Ocean Engineering*, 143(4).

Pape, L., Kuriyama, Y., and Ruessink, B. G. (2010). Models and scales for cross-shore sandbar migration. *Journal of Geophysical Research: Earth Surface*, 115(F3).

Pedrozo-Acuña, A., de Alegría-Arzaburu, A. R., Torres-Freyermuth, A., Mendoza, E., and Silva, R. (2011). Laboratory investigation of pressure gradients induced by plunging breakers. *Coastal Engineering*, 58(8):722–738.

Qi, W. G. and Gao, F. P. (2018). Wave induced instantaneously-liquefied soil depth in a non-cohesive seabed. *Ocean Engineering*, 153:412–423.

Rijn, L. C. V. and Havinga, F. J. (1995). Transport of Fine Sands by Currents and Waves. II. *Journal of Waterway, Port, Coastal, and Ocean Engineering*, 121(2):123–133.

Sakai, T. and Gotoh, H. (1996). Effect of Wave-Induced-Pressure on Seabed Configuration. In *Coastal Engineering Proceedings*, volume 1.

Sato, S., Homma, K., and Shibayama, T. (1990). Laboratory study on sand suspension due to breaking waves. *Coastal Engineering in Japan*, 33(2):219–231.

Shields, A. (1936). Application of similarity principles and turbulence research to bed-load movement. *CalTech library*.

Sui, T., Sumer, B. M., Ozgur Kirca, V. S., Carstensen, S., Zheng, J., and Fuhrman, D. R. (2023). Effect of history of wave exposure on seabed liquefaction. *Coastal Engineering*, 183:104307.

Sumer, B. M., Dixen, F., Fredsoe, J., and Sumer, S. (2006). The sequence of sediment behaviour during wave-induced liquefaction. *Sedimentology*, 53:611 – 629.

Suzuki, T., Mori, N., and Cox, D. T. (2009). Statistical modeling of near-bed pressure gradients measured on a natural beach. *Coastal Engineering Journal*, 51(2):101–121.

Suzuki, T., Shin, S., Cox, D. T., and Mori, N. (2010). Spatiotemporal Characteristics of Near-Bed Pressure Gradients on a Barred Beach. *Journal of Waterway, Port, Coastal, and Ocean Engineering*, 136(6):327–336.

Tabasi, M., Suzuki, T., and Cox, D. T. (2022). A Copula-Based Simulation of Wave-Induced Pore Water Pressure Gradient and Local Acceleration Within Surf Zone for Natural and Laboratory Barred Beach Profiles. *Frontiers in Built Environment*, 8:816020.

Tabasi, M., Yamada, M., and Suzuki, T. (2021). Laboratory Investigation of the Influence of Sediment Compaction on Wave-Induced Pore Pressure Gradient and Sediment Concentration for a Sandbar. *Journal of Japan Society of Civil Engineers, Ser. B2 (Coastal Engineering)*, 77(2):397–402.

Tang, J., Lyu, Y., Shen, Y., Zhang, M., and Su, M. (2017). Numerical study on influences of breakwater layout on coastal waves, wave-induced currents, sediment transport and beach morphological evolution. *Ocean Engineering*, 141:375–387.

Thilakarathne, S., Suzuki, T., and Mäll, M. (2024). Machine learning-driven approach to quantify the beach susceptibility to storm-induced erosion. *Coastal Engineering Journal*, 66(2):216–233.

Udden, J. A. (1914). Mechanical composition of clastic sediments. *Geological Society of America Bulletin*, 25(1):655–744.

van Kessel, T. and Kranenburg, C. (1998). Wave-induced liquefaction and flow of subaqueous mud layers. *CoasE*, 34(1):109–127.

Virtanen, P., Gommers, R., Oliphant, T. E., Haberland, M., Reddy, T., Cournapeau, D., Burovski, E., Peterson, P., Weckesser, W., Bright, J., van der Walt, S. J., Brett, M., Wilson, J., Millman, K. J., Mayorov, N., Nelson, A. R. J., Jones, E., Kern, R., Larson, E., Carey, C. J., Polat, İ., Feng, Y., Moore, E. W., VanderPlas, J., Laxalde, D., Perktold, J., Cimrman, R., Henriksen, I., Quintero, E. A., Harris, C. R., Archibald, A. M., Ribeiro, A. H., Pedregosa, F., van Mulbregt, P., Vijaykumar, A., Bardelli, A. P., Rothberg, A., Hilboll, A., Kloeckner, A., Scopatz, A., Lee, A., Rokem, A., Woods, C. N., Fulton, C., Masson, C., Häggström, C., Fitzgerald, C., Nicholson, D. A., Hagen, D. R., Pasechnik, D. V., Olivetti, E., Martin, E., Wieser, E., Silva, F., Lenders, F., Wilhelm, F., Young, G., Price, G. A., Ingold, G.-L., Allen, G. E., Lee, G. R., Audren, H., Probst, I., Dietrich, J. P., Silterra, J., Webber, J. T., Slavič, J., Nothman, J., Buchner, J., Kulick, J., Schönberger, J. L., de Miranda Cardoso, J. V., Reimer, J., Harrington, J., Rodríguez, J. L. C., Nunez-Iglesias, J., Kuczynski, J., Tritz, K., Thoma, M., Newville, M., Kümmerer, M., Bolingbroke, M., Tartre, M., Pak, M., Smith, N. J., Nowaczyk, N., Shebanov, N., Pavlyk, O., Brodtkorb, P. A., Lee, P., McGibbon, R. T., Feldbauer, R., Lewis, S., Tygier, S., Sievert, S., Vigna, S., Peterson, S., More, S., Pudlik, T., Oshima, T., Pingel, T. J., Robitaille, T. P., Spura, T., Jones, T. R., Cera, T., Leslie, T., Zito, T., Krauss, T., Upadhyay, U., Halchenko, Y. O., and Vázquez-Baeza, Y. (2020). SciPy 1.0: fundamental algorithms for scientific computing in Python. *Nature Methods*, 17(3):261–272.

Wang, L., Zhang, J., Jeng, D.-S., Zhang, Q., and Chen, T. (2023). Experimental study on the dynamic response of a silty seabed under waves. *Ocean Engineering*, 269:113554.

Wentworth, C. K. (1922). A Scale of Grade and Class Terms for Clastic Sediments. *The Journal of Geology*, 30(5):377–392.

Xu, J., Dong, J., Zhang, S., Sun, H., Li, G., Niu, J., Li, A., and Dong, P. (2022). Pore-water pressure response of a silty seabed to random wave action: Importance of low-frequency waves. *Coastal Engineering*, 178:104214.

Yang, Z., Zhu, Y., Liu, T., Sun, Z., Ling, X., and Zheng, Y. (2019). Contribution of pumping action of wave-induced pore-pressure response to development of fluid mud layer. *Journal of Marine Science and Engineering*, 7(9).

Yu, H., Liu, X., Lu, Y., Li, W., Gao, H., Wu, R., and Li, X. (2022). Characteristics of the sediment gravity flow triggered by wave-induced liquefaction on a sloping silty seabed: An experimental investigation. *Frontiers in Earth Science*, 10.

Zen, K. and Yamazaki, H. (1990). Mechanism of Wave-Induced Liquefaction and Densification in Seabed. *Soils and Foundations*, 30(4):90–104.

Zhang, S., Jia, Y., Zhang, Y., and Shan, H. (2018). Influence of Seepage Flows on the Erodibility of Fluidized Silty Sediments: Parameterization and Mechanisms. *Journal of Geophysical Research: Oceans*, 123(5):3307–3321.

Zheng, P., Gumbira, G., Li, M., van der Zanden, J., van der A, D., van der Werf, J., Chen, X., and Tang, X. (2023). Development, calibration and validation of a phase-averaged model for cross-shore sediment transport and morphodynamics on a barred beach. *Continental Shelf Research*, 258:104989.

Appendix

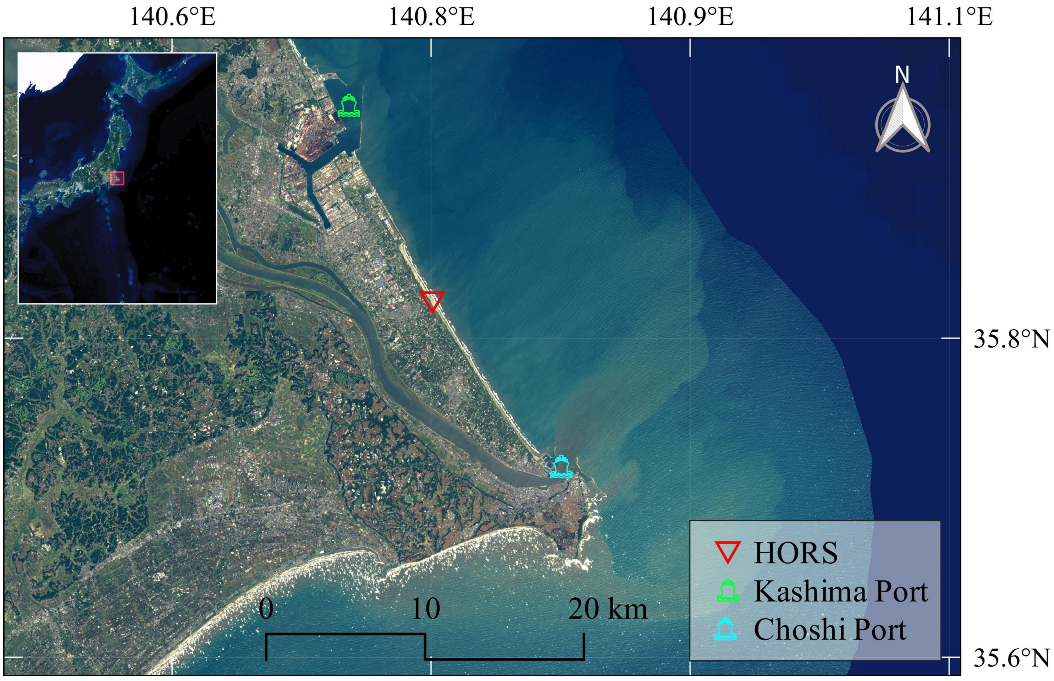

Figure A.1: Location of Hasaki oceanographic research station (HORS). Source: Thilakarathne et al. (2024)

Table A.1: Selected sandbar profiles from the field observation

Profiles (date)	**Crest from shoreline (m)**	**Cross-shore length (m)**	**Sandbar height (m)**	**Water depth above crest (m)**	**Offshore slope (deg)**	**Onshore slope (deg)**
P5 (29-09-1993)	135.1	115.82	1.45	2.19	30	33
P7 (20-12-1993)	213.33	139.99	2.22	2.53	33	35
P8 (16-09-1994)	255.33	116.67	1.82	3.19	35	30
P9 (24-09-1994)	169.77	118.65	1.70	2.19	46	10
P10 (26-09-1994)	170.06	127.12	1.51	2.20	43	6
P12 (29-10-1994)	209.89	144.07	1.51	2.86	37	21
P13 (22-01-1995)	196.11	129.95	1.60	2.79	41	22
P15 (11-03-1995)	235.31	116.39	1.43	3.38	40	30
P18 (16-09-1995)	234.46	149.72	1.43	3.53	23	24
P19 (19-09-1995)	259.04	135.60	1.93	3.83	32	34
P23 (05-05-1996)	229.66	132.77	1.70	3.11	31	34
P28 (22-01-1997)	235.59	135.60	1.51	3.19	25	36
P36 (12-09-1997)	255.65	149.72	1.68	3.35	22	32
Average	215.3	131.7	1.65	2.95	33.7	26.7
St. Dev. (σ)	38.17	12.28	0.23	0.54	7.61	9.66

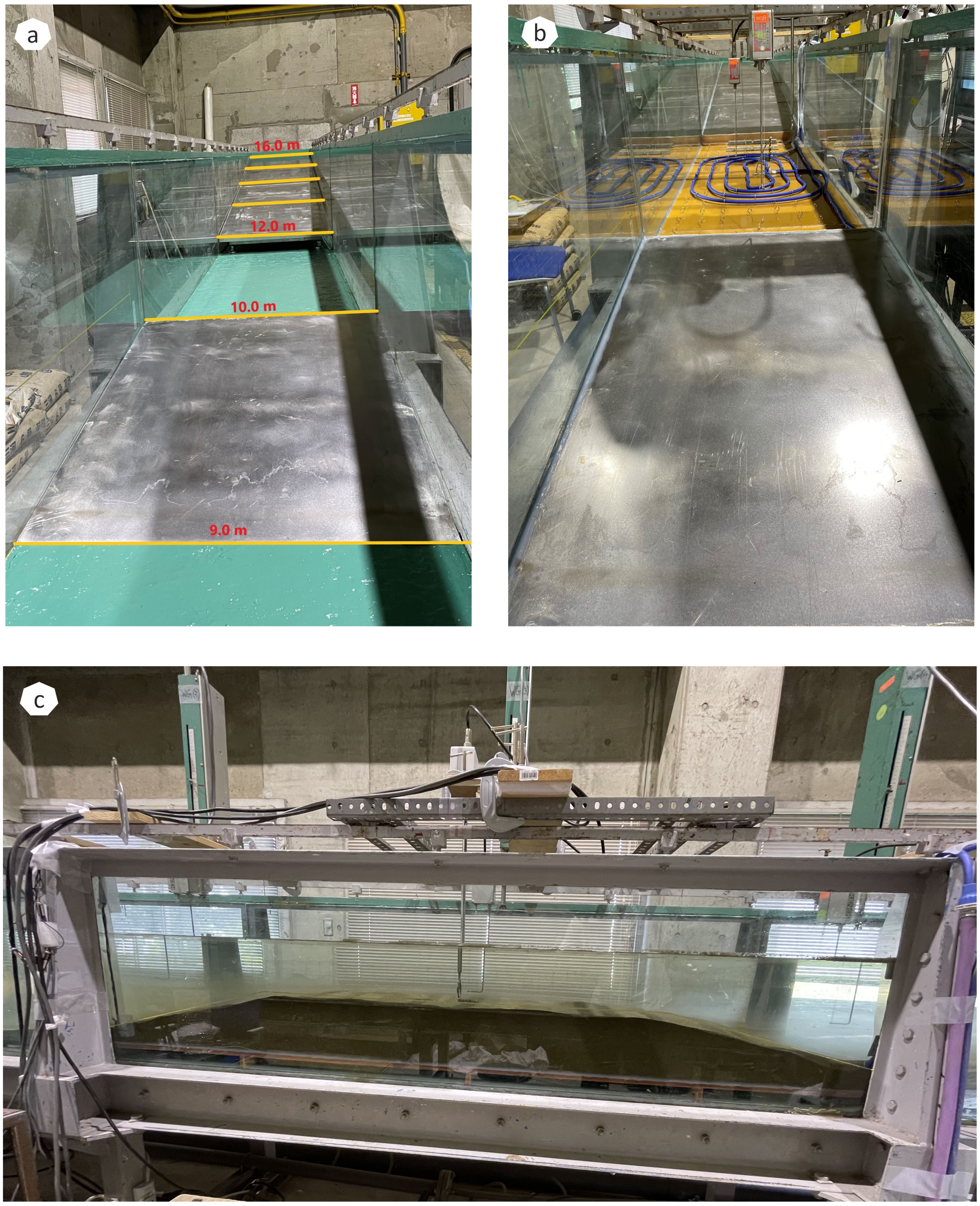

Figure A.2: Flume setup (a) before placing the wooden sandbox, (b) after installing the sandbox and instruments, and (c) after filling the sandbar area with sand.

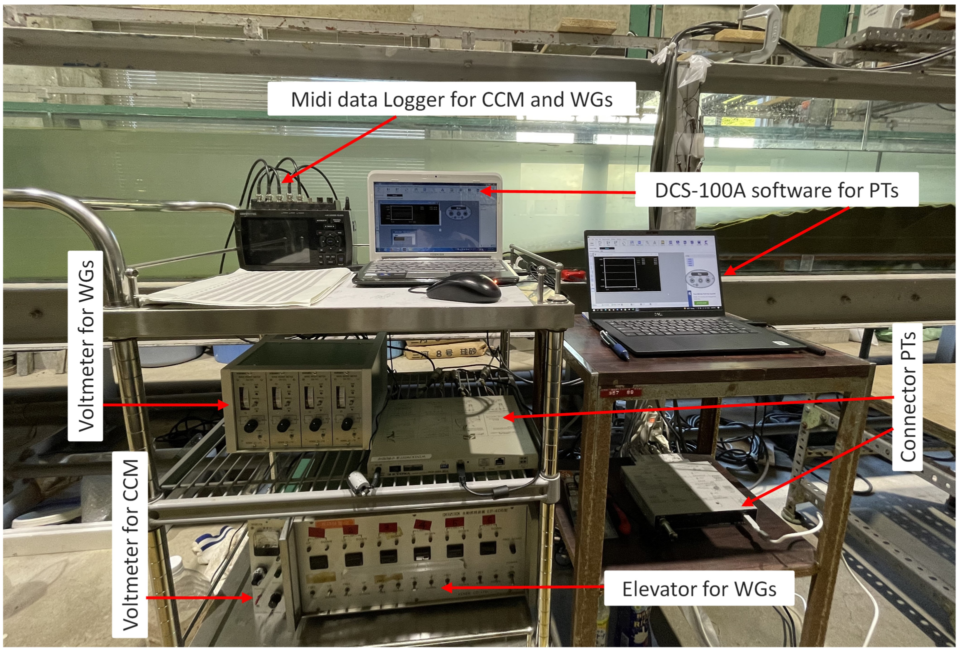

Figure A.3: Data recording unit of experimental setup.

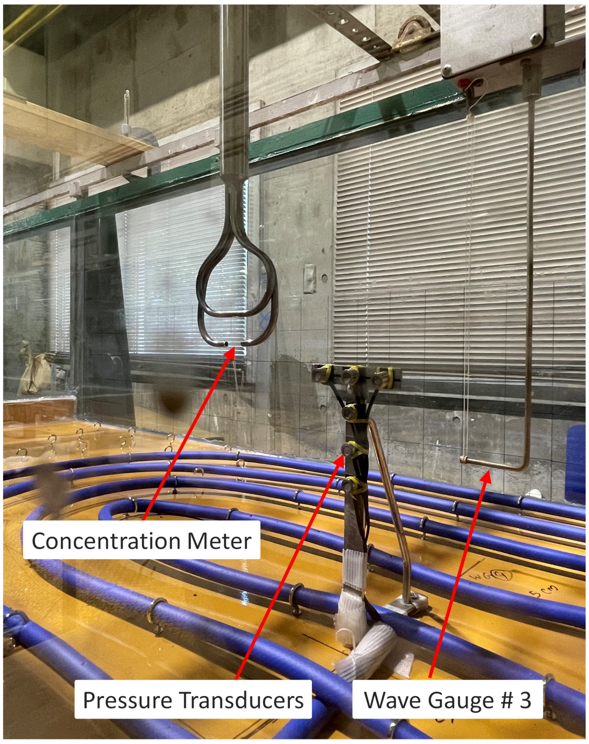

Figure A.4: Instrumental setup at cross-shore location of $x = 200$ cm: Pressure transducers, Concentration meter and Wave gauge.

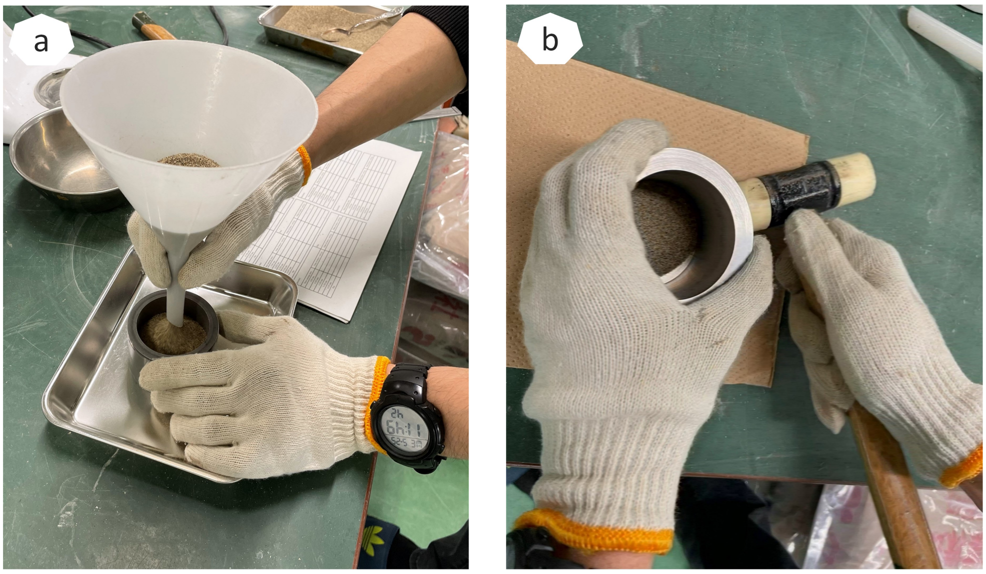

Figure A.5: (a) Minimum dry density and (b) maximum dry density measurement.

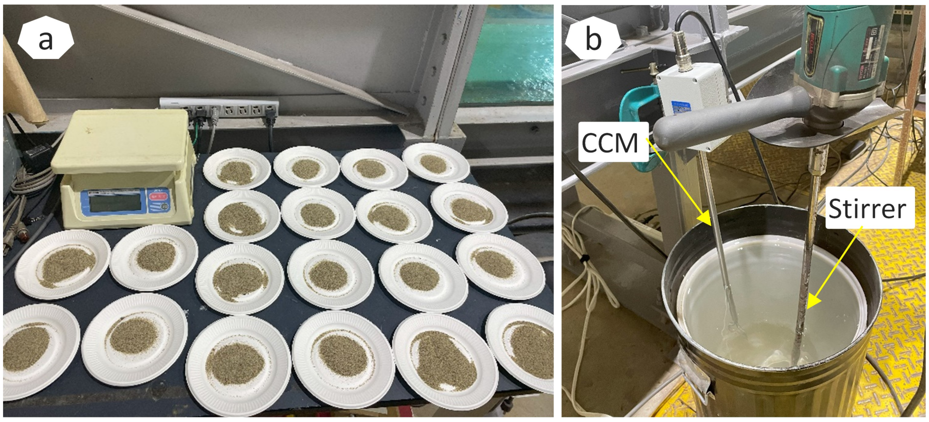

Figure A.6: Calibration process for conductivity concentration meter (CCM): (a) 20 gm sand sample and (b) CCM with mechanical stirrer.

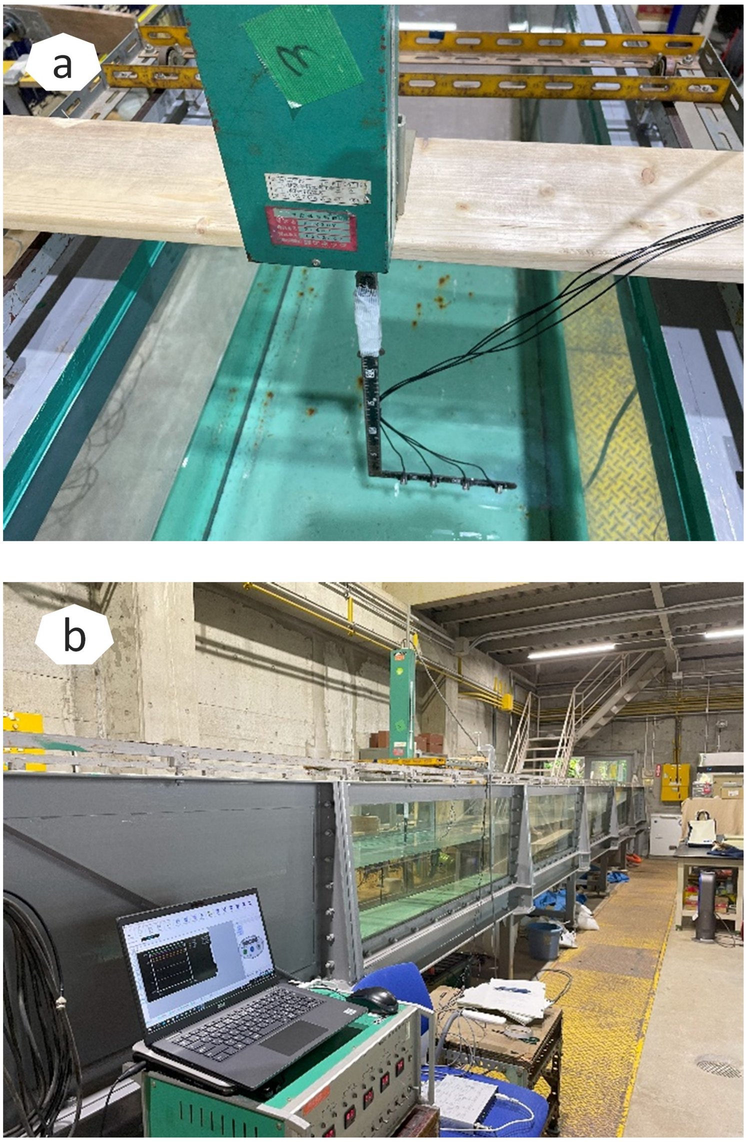

Figure A.7: Calibration process for pressure transducers (PTs): (a) PTs with the elevator and (b) data recording software (DCS-100A).

List of the Publications

Peer-reviewed Journals

Islam, M. S. and Suzuki, T. (2023). Effect of sediment size on sandbar morphology in different compaction conditions. Journal of JSCE, 11(2):23–18100. `https://doi.org/10.2208/journalofjsce.23-18100`

Islam, M. S., Suzuki, T., and Thilakarathne, S. (2024). Physical modeling of sandbar dynamics to correlate wave-induced pore pressure gradient, sediment concentration, and bed-level erosion. Ocean Engineering, 307 (2024), 118161. `https://doi.org/10.1016/j.oceaneng.2024.118161`

Kato, Y., Suzuki, T., **Islam, M. S.**, and Higa, H. (2024). Field survey of wave-induced pressure fluctuations in the sandbar layers. Journal of Japan Society of Civil Engineers, Ser. B2 (Coastal Engineering). (Accepted)

Peer-reviewed Int'l Conference Proceedings

Islam, M. S. and Suzuki, T. (2024). Quantification of wave-induced liquefaction in small-scale surf zone sandbar. In: Tajima, Y., Aoki, Si., Sato, S. (eds) Proceedings of the 11^{th} International Conference on Asian and Pacific Coasts (APAC 2023). Lecture Notes in Civil Engineering, Vol. 394, Springer, Singapore. `https://doi.org/10.1007/978-981-99-7409-2_8`

Conference/ Symposium Presentations

Islam, M. S. and Suzuki, T. Effect of sediment size on sandbar morphology in different compaction conditions. 48th Ocean Development Symposium, Hokkaido, Japan, June 28-30, 2023.

Islam, M. S. and Suzuki, T. Quantification of wave-induced liquefaction in small-scale surf zone sandbar. 11th International Conference on Asian and Pacific Coasts (APAC), Kyoto, Japan, November 14-17, 2023.